University of Nebraska - Lincoln
DigitalCommons@University of Nebraska - Lincoln

Publications, Agencies and Staff of the U.S. Department of Commerce

U.S. Department of Commerce

8-2013

Evaluation of a Cloud-Scale Lightning Data Assimilation Technique and a 3DVAR Method for the Analysis and Short-Term Forecast of the 29 June 2012 Derecho Event

ALEXANDRE O. FIERRO
University of Oklahoma Norman Campus, alex.fierro@noaa.gov

JIDONG GAO
NOAA/National Severe Storms Laboratory

CONRAD L. ZIEGLER
NOAA/National Severe Storms Laboratory

EDWARD R. MANSELL
NOAA/National Severe Storms Laboratory

DONALD R. MACGORMAN
NOAA/National Severe Storms Laboratory

See next page for additional authors

Follow this and additional works at: http://digitalcommons.unl.edu/usdeptcommercepub

FIERRO, ALEXANDRE O.; GAO, JIDONG; ZIEGLER, CONRAD L.; MANSELL, EDWARD R.; MACGORMAN, DONALD R.; and DEMBEK, SCOTT R., "Evaluation of a Cloud-Scale Lightning Data Assimilation Technique and a 3DVAR Method for the Analysis and Short-Term Forecast of the 29 June 2012 Derecho Event" (2013). *Publications, Agencies and Staff of the U.S. Department of Commerce*. 511.
http://digitalcommons.unl.edu/usdeptcommercepub/511

This Article is brought to you for free and open access by the U.S. Department of Commerce at DigitalCommons@University of Nebraska - Lincoln. It has been accepted for inclusion in Publications, Agencies and Staff of the U.S. Department of Commerce by an authorized administrator of DigitalCommons@University of Nebraska - Lincoln.

Authors
ALEXANDRE O. FIERRO, JIDONG GAO, CONRAD L. ZIEGLER, EDWARD R. MANSELL, DONALD R. MACGORMAN, and SCOTT R. DEMBEK

This article is available at DigitalCommons@University of Nebraska - Lincoln: http://digitalcommons.unl.edu/usdeptcommercepub/511

Evaluation of a Cloud-Scale Lightning Data Assimilation Technique and a 3DVAR Method for the Analysis and Short-Term Forecast of the 29 June 2012 Derecho Event

ALEXANDRE O. FIERRO

Cooperative Institute for Mesoscale Meteorological Studies, and NOAA/OAR/National Severe Storms Laboratory, University of Oklahoma, Norman, Oklahoma

JIDONG GAO, CONRAD L. ZIEGLER, EDWARD R. MANSELL, AND DONALD R. MACGORMAN

NOAA/National Severe Storms Laboratory, Norman, Oklahoma

SCOTT R. DEMBEK

Cooperative Institute for Mesoscale Meteorological Studies, University of Oklahoma, Norman, Oklahoma

(Manuscript received 2 May 2013, in final form 4 August 2013)

ABSTRACT

This work evaluates the short-term forecast (≤6 h) of the 29–30 June 2012 derecho event from the Advanced Research core of the Weather Research and Forecasting Model (WRF-ARW) when using two distinct data assimilation techniques at cloud-resolving scales (3-km horizontal grid). The first technique assimilates total lightning data using a smooth nudging function. The second method is a three-dimensional variational technique (3DVAR) that assimilates radar reflectivity and radial velocity data. A suite of sensitivity experiments revealed that the lightning assimilation was better able to capture the placement and intensity of the derecho up to 6 h of the forecast. All the simulations employing 3DVAR, however, best represented the storm's radar reflectivity structure at the analysis time. Detailed analysis revealed that a small feature in the velocity field from one of the six selected radars in the original 3DVAR experiment led to the development of spurious convection ahead of the parent mesoscale convective system, which significantly degraded the forecast. Thus, the relatively simple nudging scheme using lightning data complements the more complex variational technique. The much lower computational cost of the lightning scheme may permit its use alongside variational techniques in improving severe weather forecasts on days favorable for the development of outflow-dominated mesoscale convective systems.

1. Introduction

It is a challenging problem to numerically forecast isolated convective storms owing to the need to accurately treat complex physical interactions between dynamical and microphysical processes over a large range of scales (e.g., Stensrud et al. 2009). Mesoscale convective systems (MCSs), which consist of a grouping of isolated convective storm cells and often associate with a broad area of nonconvective or stratiform precipitation (e.g., Houze 1993; Cotton 1999), are also difficult to forecast owing to the nonlinear interactions of the component convection with the mesoscale cold pool (Ziegler 1999). MCSs occasionally do produce severe weather (e.g., Maddox 1983; Johns and Hirt 1987; Houze et al. 1990), generate over half of the annual U.S. warm season precipitation (Fritsch et al. 1986), and often produce copious cloud-to-ground (CG) lightning activity (Goodman and MacGorman 1986). Consequently, considerable attention has been recently devoted toward improving the forecast skill for storm and MCS events at cloud-resolving scales (≤4 km) using numerical weather prediction (NWP) models.

This study focuses on evaluating two distinct data assimilation techniques that are aimed at improving the initial representation (e.g., placement, intensity, and morphology) of the convection during the analysis time and subsequent short-term (i.e., ≤6 h) forecasts for the case of the 29–30 June 2012 MCS and derecho event. The first technique is a recently developed, computationally inexpensive lightning data nudging method

Corresponding author address: Alexandre O. Fierro, CIMMS, National Weather Center, Ste. 2100, 120 David L. Boren Blvd., Norman, OK 73072.
E-mail: alex.fierro@noaa.gov

DOI: 10.1175/MWR-D-13-00142.1

© 2014 American Meteorological Society

This article is a U.S. government work, and is not subject to copyright in the United States.

(Fierro et al. 2012), while the second technique is the more detailed Advanced Regional Prediction System (ARPS; Xue et al. 2001, 2003) three-dimensional variational data assimilation (3DVAR) system (Gao et al. 1999, 2004; Hu et al. 2006a,b; Stensrud and Gao 2010; Ge et al. 2010, 2012; Gao et al. 2013). The lightning data assimilation technique makes use of two-dimensional gridded total lightning flash rate densities. The 3DVAR package assimilates traditional observations as well as remote sensing data (though not lightning data at present), including three-dimensional radar reflectivity and radial velocity fields from the National Weather Service's (NWS) operational Weather Surveillance Radar-1988 Doppler (WSR-88D) network. For completeness, a summary of the current state of the knowledge in recent lightning assimilation works is first presented, followed by advances made by the community using various 3DVAR techniques with a focus on the ARPS 3DVAR package utilized herein. The chief rationale to test both lightning nudging and radar variational assimilation methods lies in the comparatively simple, computationally efficient representation of bulk storm intensity via lightning assimilation versus the much greater detail and physical robustness of radar assimilation.

Relative to the evaluation of the assimilation of observations into NWP models using variational techniques such as 3DVAR or ensemble techniques such as the ensemble Kalman filter (EnKF, e.g., Evensen 1994, 2003; Houtekamer and Mitchell 1998; Zhang 2005, 2009; Aksoy et al. 2009; Godinez et al. 2012), comparatively fewer studies have focused their attention on the assimilation of lightning data. Alexander et al. (1999) and Chang et al. (2001) were the first to demonstrate the utility of assimilating lightning data into a mesoscale model. Their work converted lightning data, from either satellite- or ground-based instruments, into a convective rainfall rate via an empirical relationship. They showed that the 12–24-h rainfall forecasts for two extratropical cyclone cases were significantly improved. Similar results were obtained a few years later by Benjamin et al. (2004) via a similar lightning assimilation procedure. Using lightning data from two ground-based networks, Mansell et al. (2007) devised a technique whereby the lightning data were allowed to control the ''trigger'' function within the Kain and Fritsch (1993) or ''KF'' convective parameterization scheme in a mesoscale model. Similar to Alexander et al. (1999), Pessi and Businger (2009) converted lightning data from the Pacific Lightning Detection Network (PacNet/LLNN) using a lightning–rainfall relationship (Jones and Macpherson 1997a,b; Alexander et al. 1999), which was then used to adjust the latent heating profile simulated by the KF scheme for a Pacific storm case. Using real-time flash-rate data from a long-range lightning detection network, Papadopoulos et al. (2005) nudged the simulated humidity profiles to empirical profiles from observed soundings during thunderstorm days to force deep moist convection into a regional mesoscale model. Following an initial idea put forth in Fierro and Reisner (2011), Fierro et al. (2012) developed a computationally inexpensive lightning assimilation technique at cloud-resolving scales whereby the model water vapor mixing ratio within the graupel-rich mixed-phase region (layer between the 0° and −20°C isotherms) is nudged as a function of the gridded total flash-rate density, the simulated graupel mixing ratio, and the ambient relative humidity. Similar to the aforementioned studies, they showed that using lightning information could significantly improve the representation of the convection at analysis time and during subsequent short-term forecasts. They noted, however, that despite their low computational cost and relative simplicity, none of the aforementioned lightning assimilation techniques account for inherent errors arising from inaccurate initial and boundary conditions in the model. While placing convection at the correct location at the initial time using lightning is relatively simple, elimination of spurious convection resulting from errors in the initial conditions of the model in a balanced manner is a far more complex issue.

Despite their relatively higher computational costs, variational methods have the chief advantage of attempting to address spurious convection. More precisely, 3DVAR produce a physically consistent three-dimensional high-resolution analysis of the model kinematic and microphysical state variables utilizing multiple data sources including observations from WSR-88Ds and the background information from the model forecast fields at a fixed time. Several 3DVAR methods have been proposed in recent years with varying degrees of application, including resolving finescale structure within severe deep convective storms (e.g., Hu et al. 2006a,b; Schenkman et al. 2011; Potvin et al. 2012), tropical cyclone prediction (e.g., Zhang et al. 2012; Hsiao et al. 2012; Li et al. 2012), heavy rainfall forecasting (e.g., Xiao et al. 2005), synoptic-scale and mesoscale applications (Barker et al. 2004), and severe weather detections and warnings (Gao et al. 2013). Several ''hybrid'' ensemble–3DVAR codes were also developed in recent years to alleviate the need to minimize a cost function and also make use of a nonisotropic flow-dependent background error covariance matrix (e.g., Etherton and Bishop 2004; Wang et al. 2007, 2008; Wang 2011). Other works have also evaluated the respective performance of 3DVAR with ensemble methods (e.g., Meng and Zhang 2008a,b) or four-dimensional variational codes (e.g., Gauthier et al. 2007). The ensemble-related data assimilation methods,

however, remain very expensive when employed within convective-scale NWP. One attractive feature of the ARPS 3DVAR package used herein is the use of multiple analysis passes with varying spatial influence scales to account for the short time-scale fluctuations of convective storms (e.g., Hu et al. 2006a,b; Gao et al. 2013). This multipass technique is reminiscent of localization approaches within EnKF codes (e.g., Zhang et al. 2009). The quality control within ARPS 3DVAR includes buddy checking, velocity dealiasing, and the removal of anomalous propagation returns. New developments for this technique include an empirical hydrometeor classification method in its observation operator for direct assimilation of radar reflectivity (Gao and Stensrud 2012), which is based on the background temperature field from the forecast of an NWP model.

It is relevant to highlight some noteworthy differences between lightning data (from either ground-based sources or satellites) and WSR-88D observations. At an elevation ranging between 3 and 6 km, WSR-88Ds provide an excellent degree of coverage of the contiguous United Stated (CONUS), while below 3 km the data usually do not overlap, resulting in an overall poor level of areal coverage (Zhang et al. 2011; Gao et al. 2013). Moreover, in contrast to lightning, radar-derived data remain scarce in oceanic region and mountainous areas. Despite this limitation, a multiradar approach utilizing this 3DVAR method during the Hazardous Weather Testbed (Clark et al. 2012) showed the overall improvement of the analysis and subsequent short-term forecasts of severe weather events (Gao et al. 2013). The chief limitation of lightning data, for its part, lies in that most current ground-based networks do not detect and locate lower-amplitude sferics from intracloud (IC) flashes, which account for the vast majority of the total flashes [2:1; Boccippio et al. (2001)], particularly within severe deep convective storms with an intracloud to cloud-to-ground (IC:CG) ratio nearing 10:1 (e.g., MacGorman et al. 1989). Unlike ground flashes, IC flashes have been shown to correlate better with convective strength and updraft development (e.g., MacGorman et al. 1989; Wiens et al. 2005; Fierro et al. 2006; Deierling and Petersen 2008), thus serving as a better proxy for thunderstorm evolution. Several recent studies have demonstrated the utility of assimilating total lightning data toward improving the analysis and short-term forecast of high-impact weather ranging from the mesoscale (e.g., Mansell et al. 2007) to the cell scale (Fierro et al. 2012). Further motivating a more systematic use of the assimilation of total lightning data is the upcoming first launch of the Geostationary Operational Environmental Satellite-R series (GOES-R; Gurka et al. 2006; Goodman et al. 2013) in 2015, which will be equipped with the Geostationary Lightning Mapper (GLM; Goodman et al. 2013), which is capable of mapping total lightning (CG + IC) day and night, year round, with a nearly uniform resolution over the Americas ranging between 8 and 12 km (Gurka et al. 2006).

2. Synoptic- and mesoscale setup of the 29 June 2012 derecho event

An exceptional, progressive derecho event (Johns and Hirt 1987, Johns and Doswell 1992) characterized by an intense bow-echo MCS produced widespread severe wind damage from the upper Midwest and Ohio River valley to the mid-Atlantic states during the afternoon and evening of 29–30 June 2012 (e.g., Vescio et al. 2013). Classical synoptic- and mesoscale ingredients supported this event (Fig. 1), including the presence of large convective instability (Fig. 1a), extreme heat and high moisture content (Figs. 1b and 1c), and strong lower-tropospheric wind shear over the area (cf. Figs. 1a and 1b, 1c). The Rapid Refresh (RAP) analysis at 1600 UTC reveals a large area of mixed-layer convective available potential energy (MLCAPE), with values exceeding 5000 J kg^{-1}, coupled with very marginal mixed-layer convective inhibition (MLCIN; <10 J kg^{-1}) over this region (Fig. 1a).

The RAP analysis and surface observations also show a quasi-stationary frontal boundary running from the upper Midwest and Ohio Valley into Pennsylvania that separated very warm and humid air to the south from relatively cooler and drier air to the north (Figs. 1b and 1c). Surface dewpoints south of this boundary (Fig. 1c) commonly reached 20°C (68°F) with maximum surface temperatures ranging between 35° and 38°C (95°–100°F) over a large area (Fig. 1b). Last and perhaps most importantly, this thermal mesoscale boundary was straddled by an upper-level northwesterly mid- and upper-level jet streak with wind speeds of about 20 m s^{-1} (40 kt) from 500 hPa (Fig. 1a) through 250 hPa (not shown). This jet streak owed its existence to the combined effects of thermal wind shear associated with the frontal zone and a high pressure circulation pattern to the south of the boundary and a low pressure system to the north centered over Ontario, Canada. Numerous high wind reports across Indiana, Ohio, West Virginia, Virginia and Maryland (including the greater Washington, D.C., metropolitan area), Pennsylvania, Delaware, and New Jersey, as well as two tornado reports in Ohio, verified the forecasted slight to moderate severe convective risk via the validated Storm Prediction Center (SPC) Day 1 Convective Outlook (Fig. 1d).

Given these rather favorable dynamic and thermodynamic ingredients (Johns and Hirt 1987; Johns and

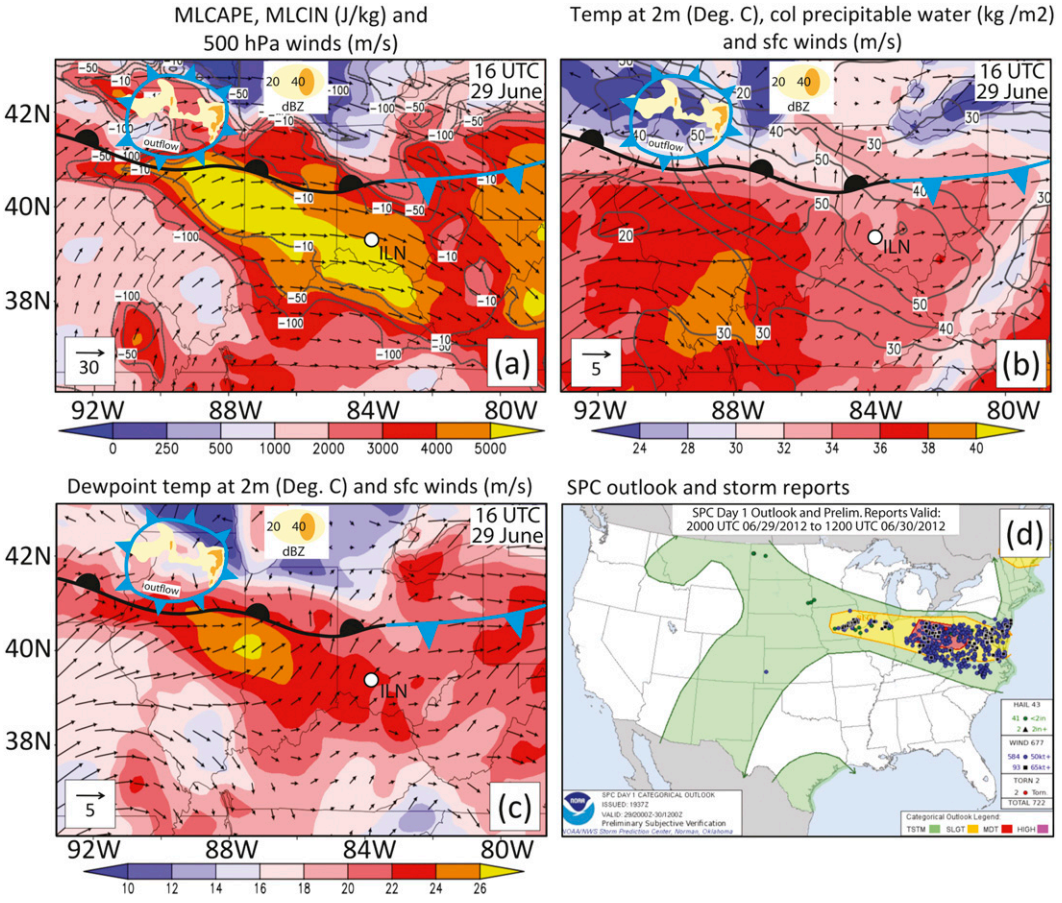

FIG. 1. (a)–(c) RAP analysis output at 1600 UTC 29 Jun 2012 and (d) the SPC validated Day 1 Convective Outlook for 29–30 Jun 2012. Color-filled MLCAPE (J kg^{-1}), contoured MLCIN (J kg^{-1}), and 500 hPa winds (m s^{-1}) are shown in (a). Color-filled temperature (°C) at 2 m AGL, contoured column precipitable water (kg m^{-2}), and surface winds (m s^{-1}) are shown in (b). Color-filled dewpoint temperature at 2 m and surface winds are shown in (c). The following mesoscale features are shown in (a)–(c): (i) positions of the surface warm front (black scalloped curve), (ii) the surface cold front (blue large-triangled curve), (iii) the color-filled areas of composite reflectivity greater than 20 and 40 dBZ at 4 km AGL and 1600 UTC, and (iv) the surface cold-pool boundary (closed, blue small-triangled curve). The vector velocity length scale (m s^{-1}) is indicated in the bottom-left corner of (a)–(c). Composite reflectivity fields are provided by the NSSL CONUS NMQ. The NWS operational sounding site at Wilmington, Ohio (ILN), is marked by a white-filled black circle.

Doswell 1992; Coniglio et al. 2004), any small-scale convective system forming near this mesoscale boundary would have a considerable probability of growing upscale into a severe MCS (and possibly a derecho). Embryonic convection that subsequently evolved into the derecho began around 1400 UTC on 29 June as a relatively small, disorganized cluster of storm cells in eastern Iowa. Near 1600 UTC (Fig. 2), the small storm cluster began rapidly organizing into a well-defined MCS that passed over Chicago, Illinois. The MCS subsequently grew upscale into an asymmetric bow echo over Indiana while moving rapidly southeastward at about 60 mi h^{-1} (~25 m s^{-1}) slightly to the north of the frontal boundary. As the MCS crossed Indiana and entered Ohio, it further intensified from a bow-echo MCS into a derecho MCS (Fig. 2). The MCS subsequently continued its destructive swath until reaching the Atlantic coast of Virginia and Maryland around 0600 UTC on 30 June (not shown). The Storm Prediction Center (SPC) estimated a damaging wind swath of about 1000 km in length, with over 800 wind damage reports alone during the 10-h lifetime of the event (e.g., Figs. 1d and 2). Severe wind gust reports ranging between 60 and 70 mi h^{-1} (~25–33 m s^{-1}) were widespread with peak gusts in excess of 90 mi h^{-1} (40 m s^{-1}) reported over eastern Indiana and western Ohio (Fig. 2). At least 22 fatalities and loss of power to over 5 million customers were attributed to this event. According to the National Climatic Data Center, the preliminary damage cost estimate of this derecho exceeded several hundred million to a billion U.S. dollars

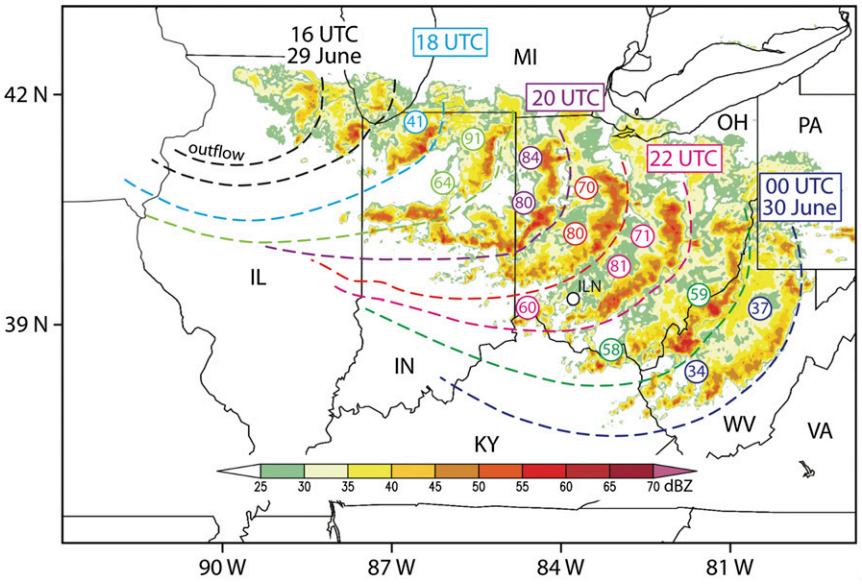

FIG. 2. Hourly evolution of composite radar reflectivity (dBZ) at 4 km AGL of the derecho-producing MCS during the period 1600 UTC 29 Jun–0000 UTC 30 Jun 2012. The colored dashed curves denote the hourly positions of the leading edge of the cold-pool boundary near the surface as inferred from clear-air NSSL mosaic reflectivity fields. Preliminary observed wind gusts (mi h^{-1}) are at approximate locations during the hour previous to the indicated times (G. Carbin, SPC, 2013, personal communication). Outflow boundaries, wind gusts (if any), and their time labels are all colored consistently to discriminate evolution. The NWS operational sounding site at Wilmington, Ohio (ILN), is shown by a white-filled black circle.

(http://www.ncdc.noaa.gov/billions/events). Local newspapers in Ohio (including the *Columbus Dispatch*) reported insured losses reaching almost $1 billion, making it the third-most expensive natural disaster in Ohio in 38 years. In Virginia, power outages (~1 million) were the third largest ever after Hurricanes Isabel (2003) and Irene (2011).

3. Simulation setup

The model used in this study is the three-dimensional compressible nonhydrostatic Weather Research and Forecasting Model (WRF version 3.3.1) with the Advanced Research WRF (ARW) dynamic solver (WRF-ARW; Skamarock and Klemp 2007). The overall model setup has been designed to mimic routine experimental real-time forecasts conducted with the National Severe Storms Laboratory (NSSL) 4–km WRF-ARW test bed over CONUS (Kain et al. 2010).

a. Model grid and physics configuration

The simulation domain (D01; Fig. 3) has a uniform horizontal grid spacing of 3 km and horizontal dimensions in grid points of 1001 × 501. The stretched vertical grid has 35 levels with its model top set at 50 hPa (~20 km). The initial and time-dependent lateral boundary conditions employ the 3-hourly, 12-km North American Mesoscale Model (NAM) operational analysis data (1200 UTC 29 June 2012 run) for a 18-h period starting at 1200 UTC on 29 June 2012. The computational time step is set to 15 s.

The simulations employ the WRF single-moment, 6-class bulk microphysical scheme of Hong and Lim (2006; WSM6). The six bulk species are rain, cloud water, cloud ice, snow, graupel, and hail. The boundary layer is parameterized following the Eta implementation of the 1.5-order closure Mellor–Yamada scheme (Mellor and Yamada 1982) and the turbulence kinetic energy scheme adapted by Janjić (1994) with Monin–Obukhov–Janjić similarity theory for the subgrid-scale turbulence processes (Chen et al. 1997). Lower boundary conditions for turbulent fluxes are provided by the unified Noah land surface model (Chen and Dudhia 2001; Ek et al. 2003). The longwave and shortwave radiation are both parameterized following the Goddard scheme [adapted from Mlawer et al. (1997)].

b. Data assimilation procedures

The lightning data used in this work are provided by the Earth Networks Total Lightning Network (ENTLN), which consists of over 150 sensors deployed over CONUS and is able to detect both IC and CG flashes with a national-average detection efficiency exceeding 95% for

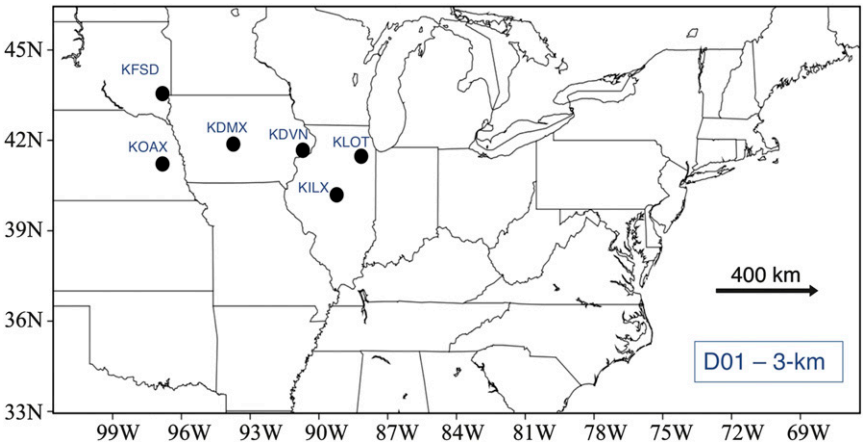

FIG. 3. Sketch of the simulation domain, D01 (3-km grid spacing) with the black dots denoting the locations of the WSR-88D sites used and tested in the ARPS 3DVAR code herein.

typical CG return strokes and about 50% for typical IC flashes (see Fig. 6 in Fierro et al. 2012). The ENTLN location accuracy varies from tens of meters in dense areas of the network to about 500 m elsewhere. The cloud-scale lightning assimilation technique follows Fierro et al. (2012), whereby incremental increases in water vapor mixing ratio in the graupel-rich layer between 0° and −20°C are applied at observed lightning locations. The nudging-induced increase in water vapor mass at a grid point is proportional to the observed gridded flash-rate density (per 3-km grid cell herein) and inversely proportional to the simulated graupel mixing ratio at that grid point (threshold for zero nudging also set to $3\,g\,kg^{-1}$). The nudging from lightning data is only applied at lightning locations with relative humidity values below 80% in the model. Lightning was assimilated during a 2-h period between 1400 and 1600 UTC on 29 June, which covers the development of the embryonic thunderstorm clusters in eastern Iowa and northern Illinois (e.g., Figs. 4a–c), just prior to the start of the upscale growth of the system (Fig. 2). Similar to Fierro et al. (2012), the lightning data (hourly rates shown in Figs. 4d–f) are binned into 10-min intervals to reasonably resolve storm motion while the nudging of water vapor is maintained throughout the 10-min interval at each computational time step until switching to the next 10-min interval.

The ARPS 3DVAR system, especially designed for storm-scale data assimilation, uses a recursive filter (Purser et al. 2003a,b) with a mass continuity equation and other constraints that are incorporated into a cost function, yielding three-dimensional analyses of the wind components and other model variables. Multiple analysis passes are used that have different spatial influence scales to accurately represent intermittent convective storms, and the quality control steps within the ARPS 3DVAR scheme also are critical for the radial velocity and reflectivity data. The 3DVAR analysis step is followed by a cloud analysis package that uses radar reflectivity and other cloud observations. The package was initially based on the Local Analysis and Prediction System (LAPS; Albers et al. 1996) and subsequently modified for the ARPS system (Zhang et al. 1998; Brewster 2002; Hu et al. 2006a). The mixing ratio of precipitation (including rainwater, snow, and hail) and potential temperature are adjusted within the cloud analysis based on reflectivity measurements. No adjustments are made to the other hydrometeor variables to avoid potential negative impacts of these adjustments on the balance of model equations during the analysis cycle. By using observations from two or more WSR-88Ds scanning the same atmospheric volume simultaneously (particularly where radars overlap between 3 and 6 km AGL), it is possible to analyze a full three-dimensional wind field from the radial velocity data alone.

The 3DVAR assimilation procedure (Gao et al. 2013) makes use of the WSR-88D level II data that have been obtained from the National Climatic Data Center (http://www.ncdc.noaa.gov/oa/radar/radardata.html). For this study, radar reflectivity and radial velocity data from six radar sites have been employed (Fig. 3). The rationale behind the choice of these particular radar sites is to reasonably capture the development of the embryonic thunderstorm clusters in eastern Iowa and northern Illinois between 1400 and 1600 UTC (Fig. 4). Other experiments using two additional radar sites in the pre-derecho environment [namely, Indianapolis (KIND) in central Indiana and Wilmington (KILN) in west-central Ohio] have been conducted (not shown), and have demonstrated very similar results to those obtained with the base set of six radars in Fig. 3. For consistency, the

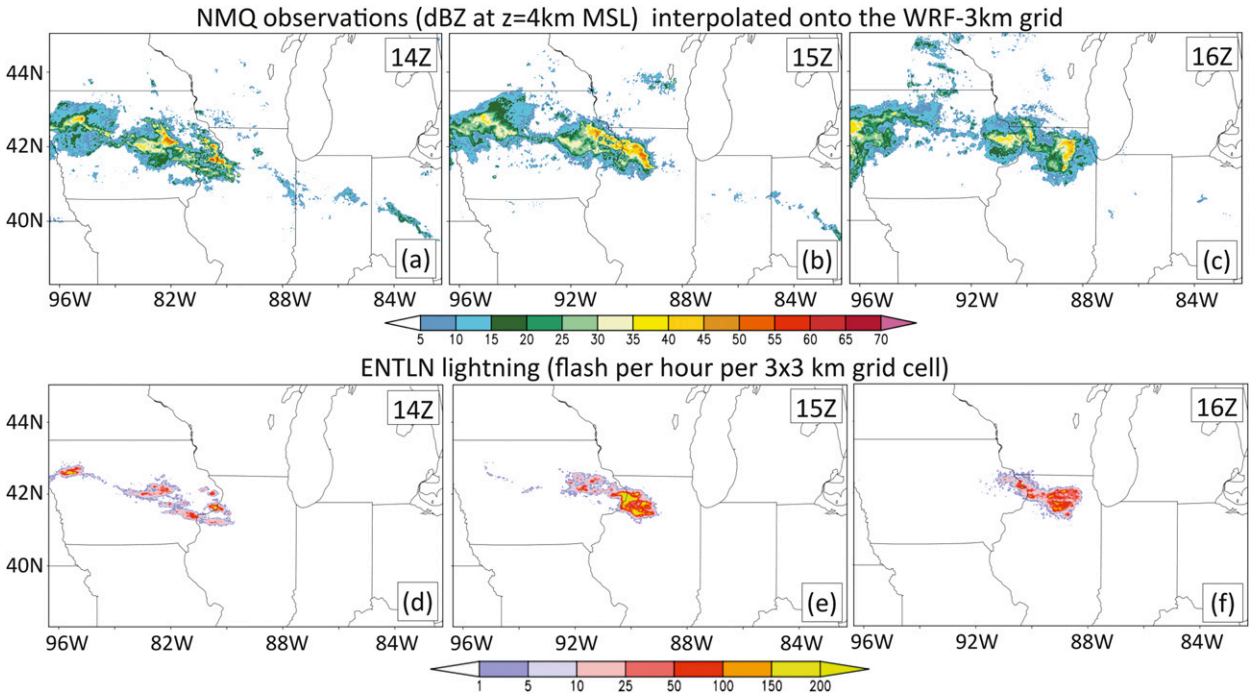

FIG. 4. Radar reflectivity (dBZ) and lightning observations between 1400 and 1600 UTC 29 Jun 2012, which spans the early stage of the formation of the derecho MCS (see also Fig. 2) and the period selected for assimilation. Horizontal cross section of radar reflectivity at 4 km AGL from the 1-km resolution, 3D NMQ product interpolated onto the local 3-km D01 domain at (a) 1400, (b) 1500, and (c) 1600 UTC on 29 Jun 2012. (d)–(f) As in (a)–(c), but for the hourly lightning flash densities on D01 (flash per hour per 3 km × 3 km grid cell) up to the time shown on the figure. Legends for colors and shadings are shown at the bottom of each row.

3DVAR assimilation is performed during the same 2-h period as the ENTLN lightning assimilation. Owing to the computational expense dictated by the relatively large model grid used herein ($\sim 1.75 \times 10^7$ grid cells), the frequency of the 3DVAR cycles is set to 30 min. An additional 3DVAR sensitivity experiment was carried out using a 10-min assimilation cycle frequency (not shown) that confirmed qualitatively similar behavior to that with a 30-min cycle. Unless otherwise specified, all 3DVAR runs make use of the cloud analysis package (Hu et al. 2006a,b) during the assimilation of the radar reflectivity data. Observed reflectivities below a threshold of 15 dBZ are not included in the 3DVAR to reduce any unwanted influence of weak radar returns or ground clutter. The effective influence radius of a radar site is set to 230 km with each data point having an influence radius set at 21 km.

Though the 3DVAR package was developed for the ARPS model, it has been adapted for use by WRF via an interface between the two models according to the following procedure. The first step linearly interpolates WRF output onto the ARPS model grid. The obtained product serves as a background field for the 3DVAR analysis. Radar data are then quality controlled (e.g., dealiasing radial velocity, removing ground clutter) and interpolated onto the ARPS grid in the second step. The third step implements the 3DVAR analysis by using background and radial velocity data to update the three Cartesian wind field components. The potential temperature (θ), water vapor mixing ratio (q_v), the atmospheric pressure, and the hydrometeor variables (i.e., cloud water and cloud ice, rain, snow, and graupel/hail mixing ratios) are all updated by the cloud analysis following the 3DVAR analysis. The fourth step interpolates the analysis results from the ARPS grid onto the WRF grid. In the final step, WRF is integrated for 30 min to complete one 3DVAR data assimilation cycle. The above procedure is repeated 5 times (given 30-min cycles) from 1400 to 1600 UTC.

The WRF-forecasted radar reflectivity fields are evaluated against the NSSL's three-dimensional National Mosaic and Multisensor Quantitative Precipitation Estimation (QPE) or 3D NMQ product (Zhang et al. 2011). The 1-km NMQ composite reflectivity is spatially interpolated onto the 3-km model grid, as previously described by Fierro et al. (2012).

Additional preliminary model tests have demonstrated that starting the assimilation (3DVAR and/or lightning) at 1200 UTC instead of 1400 UTC has negligible effects on the forecast and on the representation (location and intensity) of the convection at analysis time. The probable

TABLE 1. List of the nomenclature/abbreviations for the simulations conducted and described in this study. The right column indicates the type of data that were assimilated, with dBZ standing for radar reflectivity and Vr for radial velocity.

Simulations	Description	Data assimilated
CTRL	Control run	None
LIGHT	Lightning assimilation run	ENTLN lightning densities
ALL	3DVAR run using all six radar sites in Fig. 3	dBZ and Vr
4RAD	3DVAR run using the four westernmost radar sites of Fig. 3	dBZ and Vr
4RAD+ILX	As in 4RAD, but with the addition of the KILX radar	dBZ and Vr
4RAD+LOT	As in 4RAD, but with the addition of the KLOT radar	dBZ and Vr
ILX	3DVAR run only with the KILX radar	dBZ and Vr
ILX-DBZ	As in ILX, but without Vr data	dBZ
ILX-VR	As in ILX, but without dBZ data	Vr

reason for the latter lack of sensitivity is that prior to 1400 UTC all of the convective cells that developed in western and central Iowa decayed rapidly and were not associated with the storm cluster in eastern Iowa that quickly intensified and grew upscale to form the derecho MCS.

4. Results

a. Base runs

In this section, the performance of the lightning data assimilation scheme (LIGHT) and ARPS 3DVAR using all six radar sites (ALL; Fig. 3) are first evaluated against observations and a control run (CTRL), whereby the model is advanced unconstrained without assimilating any data. For the sake of brevity, this analysis solely focuses on the main derecho event and does not consider remote convection present in the observations. The acronyms representing the simulations are listed in Table 1.

When neither lightning nor radar data are assimilated (CTRL), the model fails to initiate convection at 1600 UTC in eastern Iowa and northern Illinois (cf. Figs. 5a and 5d). Instead, CTRL develops a thunderstorm cluster near the observed location of the embryonic MCS derecho 3 h later in the simulation (cf. Figs. 5b and 5e) that moves east-southeastward with other, later storms that develop ahead of its leading edge in southern Ohio (cf. Figs. 5c and 5f). Both LIGHT (cf. Figs. 5a–c and 5g–i) and ALL (cf. Figs. 5a–c and 5j–l) clearly outperformed CTRL. At analysis time (1600 UTC), ALL generates a reflectivity structure of the embryonic MCS that is forced toward the observations yet displaced slightly to the south (cf. Figs. 5a and 5j), while the LIGHT-generated MCS lacks weaker reflectivities and appears to be rather more convective in nature than suggested by the observed reflectivities (cf. Figs. 5a and 5g). The formation of the spurious convection ahead of the parent MCS in ALL at the 3-h forecast further exacerbates the southward displacement error of the leading edge of the MCS. In the 3- and 6-h forecasts, the MCS produced by LIGHT (Figs. 5h and 5i) is in better agreement with the observations (Figs. 5b and 5c) than the ALL-generated MCS (Figs. 5k and 5l). The ALL-generated MCS in the 6-h forecast appears more convective than LIGHT with a comparatively smaller areal coverage of reflectivity values below 40 dBZ (cf. Figs. 5i and 5l). A spurious cluster of thunderstorms is produced by ALL ahead of the intensifying parent MCS beginning around 1700–1800 UTC (i.e., 1–2 h into the forecast), as evidenced by unobserved convection over southeastern Indiana (cf. Figs. 5k and 5b). The spurious convection over Indiana subsequently leads to the early demise of the parent MCS (cf. Figs. 5k and 5b). Eventually, the spurious thunderstorm cluster forms a new convective system ahead of the original MCS before intensifying and moving east-southeastward (cf. Figs. 5l and 5c). This spurious discrete propagation episode explains why the ALL-simulated MCS is further displaced to the east compared to the LIGHT-simulated MCS at the 6-h forecast time (cf. Figs. 5i and 5l).

As indicated by the inferred location of the leading edge of the outflow boundary (Fig. 5 and also shown in Fig. 2), at 3 h (6 h) the LIGHT-simulated MCS forecast exhibits a noteworthy southward (southeastward) displacement from the observations. One potential factor for this disparity might be the overestimation of evaporation rates in the subcloud layer of the MCS produced by the WSM6 microphysics scheme, which would force an overly intense mesoscale cold pool and density current propagating too quickly against the ambient southwesterly surface winds (e.g., Ziegler et al. 2010; Van Weverberg et al. 2013). The overall lack of a stratiform region in the simulated MCS is also noted. A possible cause of this too little stratiform precipitation area is the inability of single-moment schemes to accurately simulate transitions from regions of high concentration of small particles to relatively low concentrations of larger particles associated with ice growth via deposition,

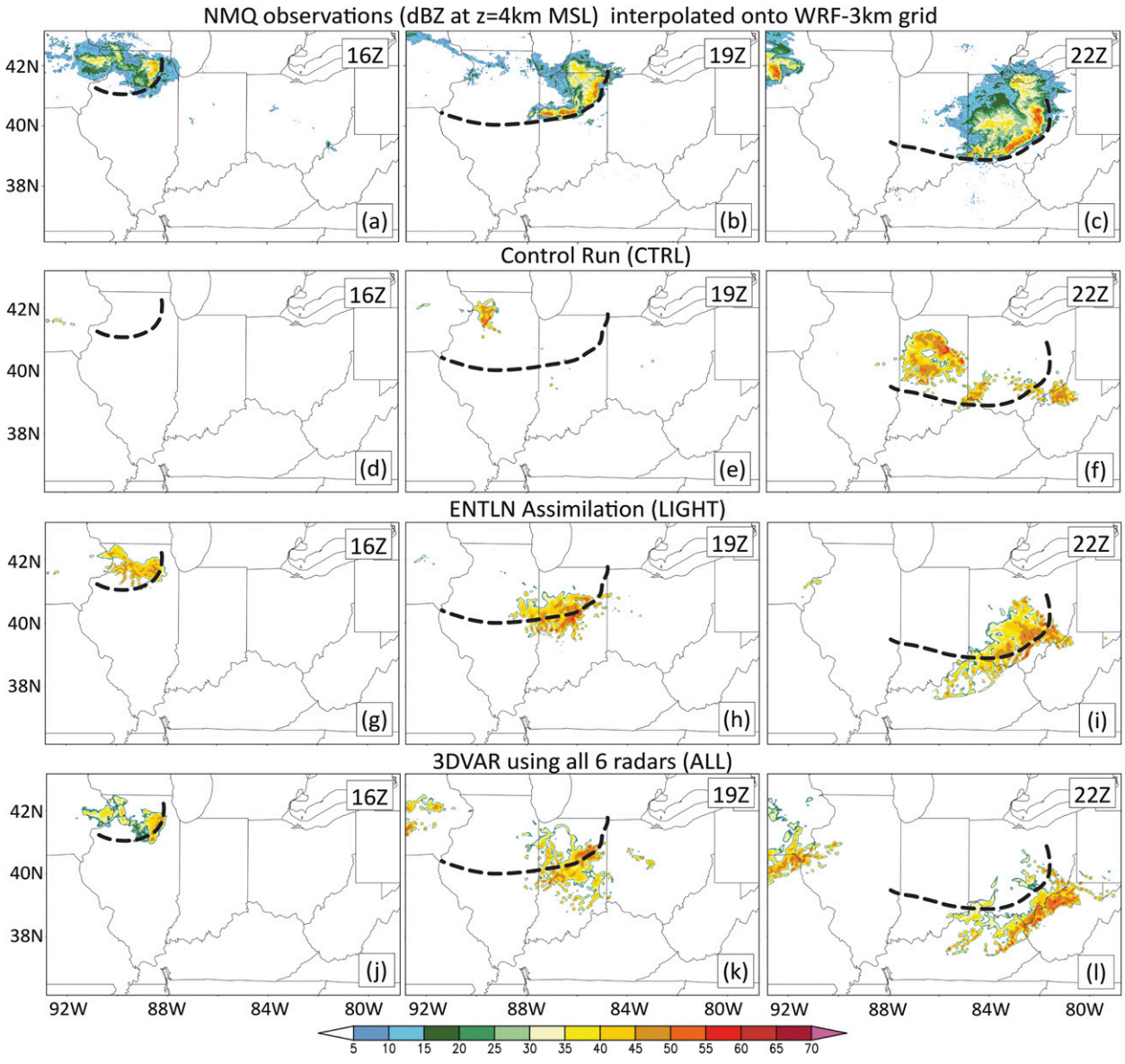

FIG. 5. Observed and modeled reflectivity fields (dBZ) at 4 km AGL. The top row is as in Figs. 4a–c but at (a) 1600, (b) 1900, and (c) 2200 UTC 29 Jun 2012. For clarity and consistency, all subsequent plots are zoomed over a subset of D01 covering parts of eastern Iowa and the Ohio Valley where the derecho formed and grew upscale. (d)–(f) Results from CTRL. (g)–(i) As in (d)–(f), but for LIGHT. (j)–(l) As in (g)–(i), but for the 3DVAR assimilation run ALL. The thick, black-dashed curves denote the positions of the leading edge of the cold-pool boundary near the surface as inferred from clear-air NSSL mosaic reflectivity fields, as in Fig. 2. Legends for colors and shadings are shown at the bottom of the figure.

aggregation, and riming (e.g., Passarelli 1978, Rogers and Yau 1989, Bryan and Morrison 2012) or, as mentioned in Fierro et al. (2012), that neither low-density graupel nor aggregate are well represented in single-moment schemes.

A comparison of the 3-hourly sequences of perturbation potential temperature θ' at the lowest model level (referred to as surface level) and 10-m wind speeds (Figs. 6 and 7, respectively) helps to illustrate the diverging evolutions of the LIGHT- and ALL-generated MCSs. The evolution of the simulated MCS is well represented by the surface θ' and 10-m winds, which characterize the intensity of the MCS derecho's cold pool that in turn forces the regeneration of leading-line convection. The presence of the spurious thunderstorm cluster in southeastern Indiana ahead of the main MCS derecho in ALL is evident in the spurious cold-pool temperature perturbation (cf. Figs. 6e and 6h) and the

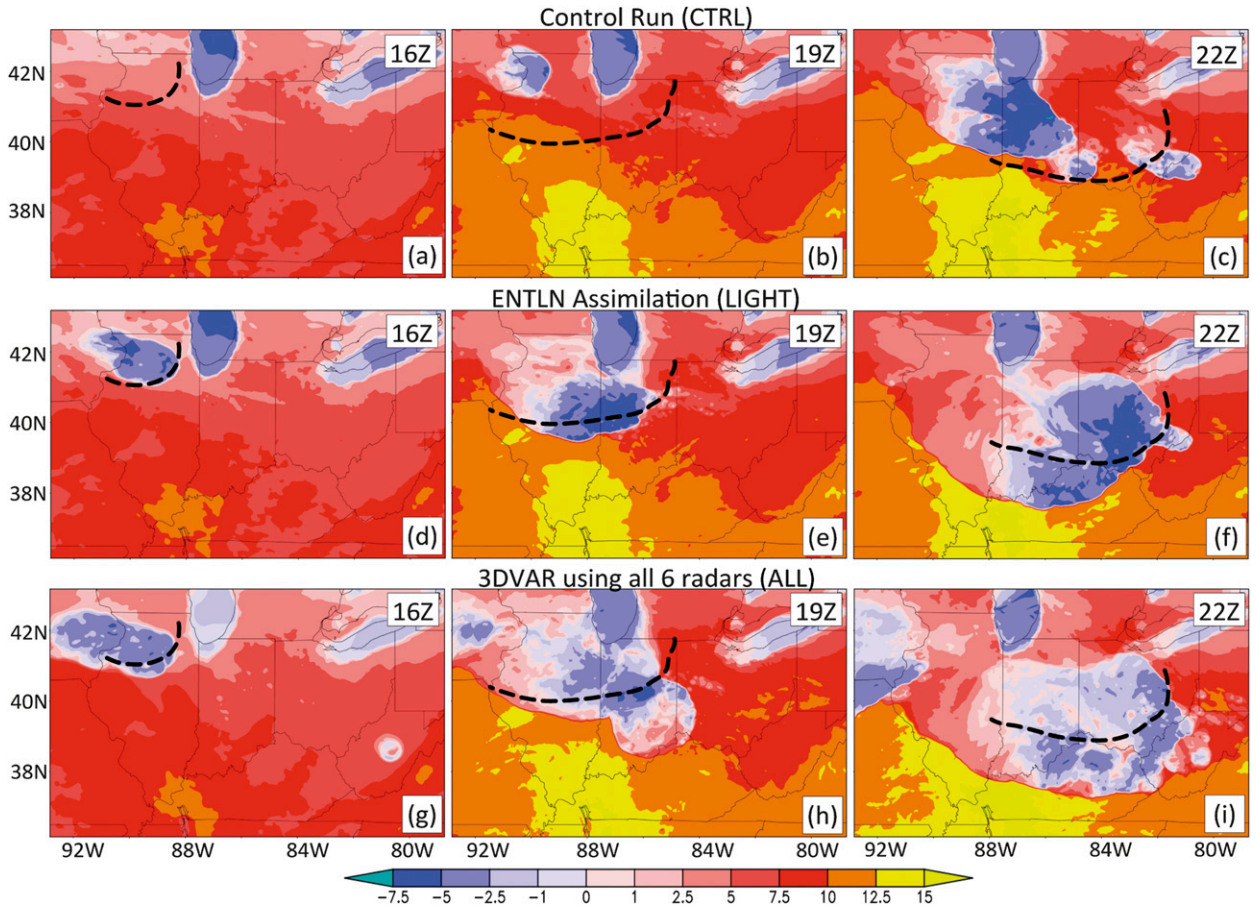

FIG. 6. As in Figs. 5d–l, but depicting the perturbation potential temperature (K) at the lowest model level.

10-m winds (cf. Figs. 7e and 7h), respectively. The effects of the development of this spurious storm cluster on the subsequent intensity of the parent MCS are also more evident later in the forecast. For example, at 2200 UTC LIGHT exhibits a well-defined cold pool with θ' values commonly ranging between -5 and -7.5 K (Fig. 6f). In contrast, the cold pool in ALL seldom exhibits θ' values smaller than -5 K (cf. Figs. 6f and 6i). The smaller area of the -5 K contour in the simulated cold pool in ALL compared to LIGHT is consistent with (i) a modeled smaller areal coverage of reflectivities exceeding 30 dBZ at $z = 4$ km (cf. Figs. 5i and 5l) and (ii) the weakening of the parent MCS at 1900 UTC, as evidenced by smaller reflectivity values within its leading edge in central Indiana (Fig. 5k). Figure 6 further highlights that by 2200 UTC (6-h forecast), the trailing edge of the cold outflow boundary is located farther south into central Kentucky in both the LIGHT and ALL forecasts relative to its inferred location derived from the observed reflectivity fields and surface observations (Fig. 6f and 6i).

The simulated 10-m wind speeds in the MCS derecho are stronger for LIGHT than ALL through all respective forecast periods (Figs. 7e, 7f, 7h, and 7i), and peak wind speeds in the LIGHT forecast are most closely consistent with peak reported surface gusts of up to 36 m s^{-1} (Fig. 2). The highest 10-m wind speeds in both the LIGHT and ALL forecasts are contained within a series of surge lines (Figs. 7e, 7f, and 7i), whose rather small scale implies the difficulty of validating their detailed structure due to the relatively poor spatial resolution of the existing operational surface network. At the 3-h forecast (1900 UTC), the spurious storm cluster in ALL leads to the weakening of the 10-m winds of the parent MCS, which results in peak values seldom exceeding 20 m s^{-1} (Fig. 7h). In contrast, the LIGHT storm at 1900 UTC exhibits wind speeds commonly in excess of 25 m s^{-1} with the 20–25 m s^{-1} contour covering a larger area (and, hence, larger damaging wind swath; cf. Figs. 7e and 7h). In contrast to ALL and CTRL, LIGHT produces a prominent feature of warmer potential temperature anomalies at the 6-h forecast in the subcloud layer (i.e., θ' values ranging from

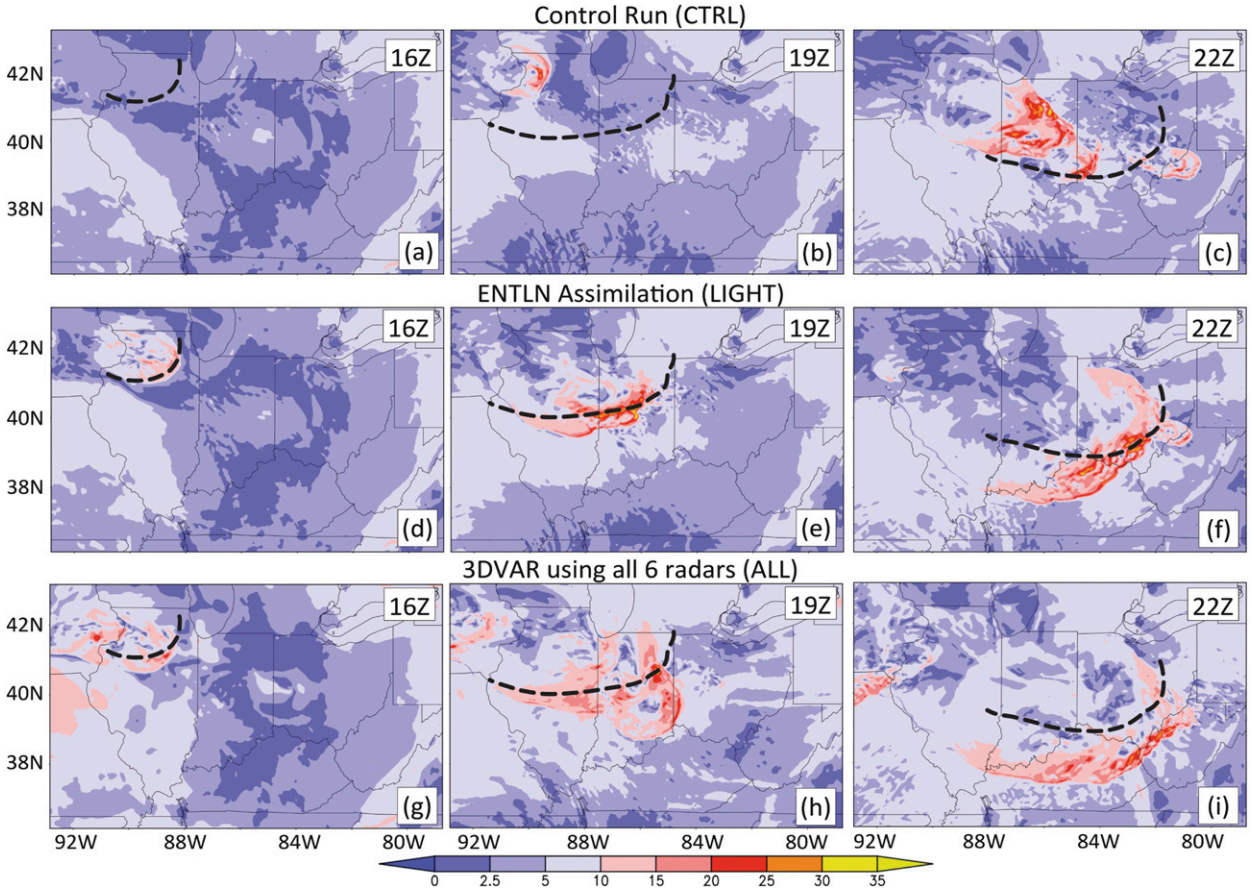

FIG. 7. As in Figs. 5d–l, but depicting the wind speeds ($m\,s^{-1}$) interpolated at 10 m AGL.

+7.5 to +10 K; at 500 m MSL, not shown) within its cold pool over southeast Indiana that is collocated with the simulated MCS's descending rear-to-front inflow reflectivity notch. Additional detailed analysis of vertical cross sections (not shown) reveal that this warm tongue arises from the fast descent of air parcels with adiabatic warming that are transported through a classical descending rear-inflow jet (RIJ), a feature often detected in radar-observed bow-echo MCSs (e.g., Wakimoto et al. 2006). The tip of this warm tongue at the base of the RIJ is coincident with local wind speed maxima in excess of 25–30 $m\,s^{-1}$ (Fig. 7f) just behind the leading edge of the simulated cold pool (Fig. 6f). It is hypothesized that the stronger mesoscale cold pool in LIGHT may have contributed to the MCS intensifying further compared to ALL (e.g., Xu et al. 1996; Xue et al. 1997). This latter result (and thus the hypothesis) holds even when the spurious MCS is eliminated in one of the subsequent 3DVAR experiments (described later in this section).

Relevant information can be deduced from analyzing the general morphology and evolution of the simulated convection (Fig. 5). Regardless of whether the model-generated storm cluster at 3 h is at the observed location (LIGHT; Fig. 5h) or else is displaced (CTRL, Fig. 5e; ALL, Fig. 5k), the convective cluster in any event grows upscale and intensifies into a well-defined, strong outflow-dominated MCS (see Figs. 5d–f, 6a–c, and 7a–c for CTRL results). As previously hypothesized in section 1, the model's large-scale environment that was advanced from initial conditions derived from the 12-km NAM dataset appears to reasonably capture the environmental conditions favorable for the occurrence of a strong MCS-induced derecho wind event. A detailed hourly analysis of the evolution of the large-scale fields in the WRF output and RAP analysis data from 1200 UTC 29 June through 0600 UTC 30 June (not shown) reveals that this was indeed the case. As previously illustrated at 1600 UTC (Fig. 1), the mesoscale prestorm environment near and ahead of the advancing MCS is characterized by widespread large MLCAPE values (~5000 $J\,kg^{-1}$), high relative humidity (80%–95%), high dewpoints (18°–22°C), and a strong midtropospheric zonal jet stream at upper levels straddling a weak thermal boundary at low levels in the Ohio River valley. Therefore, the

introduction of a sufficiently intense small-scale convectively induced cold-pool perturbation (whether real or spurious) into an environment possessing such strongly favorable ingredients would likely initiate deep, moist convection that would grow upscale and significantly alter the outcome of the forecast (as demonstrated in the ALL forecast). In other words, viewing this case via the paradigm of a semichaotic ''decision point'' within a mesoscale-environmental ''attractor'' (e.g., Stensrud and Bao 1992) suggests that the total forecast error due to the spurious convection initiation (CI) ahead of the MCS (i.e., the decision point) may be bounded by the extremely favorable ambient mesoscale state of the present derecho-supporting environment.

Prior tests for this convective event have revealed that simultaneously using the lightning nudging technique and the 3DVAR scheme have led to a WRF solution that is very similar to the solution obtained using assimilated lightning data alone. This result may not be surprising given that the lightning nudging is applied at every computational time step to maintain a cell-scale secondary circulation at the observed lightning locations (Fierro et al. 2012), whereas the 3DVAR is conducted every 30 min primarily owing to its high computational cost and also to the frequency of available level II WSR-88D data (i.e., ~5-min radar volume spacing).

b. *Sensitivity to the radar sites used*

To examine in more detail what factor(s) might lead to the formation of a spurious storm cluster ahead of the parent MCS in ALL, six additional 3DVAR initialization sensitivity tests were carried out. The first group of three tests aims at identifying which radar(s) among the six sites used herein (Fig. 3) leads to a spurious mesoscale prestorm environmental perturbation leading to CI. Toward this goal, the above 3DVAR experiment (ALL) was rerun with the following restrictions: (i) only the four westernmost radars [Omaha, Nebraska (KOAX); Des Moines, Iowa (KDMX); Sioux Falls, South Dakota (KFSD); and Quad Cities, Iowa (KDVN), in Fig. 3] were used (run 4RAD); (ii) the same radars were used as in 4RAD, but with Lincoln, Illinois (KILX) added (4RAD+ILX); and (iii) as in 4RAD, but with Chicago, Illinois (KLOT), added (4RAD+LOT). These three radar site combinations were selected because the radar locations are consistent with the 3DVAR effective influence radius selected for this study (i.e., 230 km). Reasoning that the spurious convective cluster develops near central Indiana, the most likely radar candidates to produce spurious CI-forcing perturbations (i.e., those radars within range of the spurious CI) are KLOT and KILX.

The spurious storm cluster in southeastern Indiana does not appear in 4RAD, which facilitates an uninterrupted, progressive intensification and upscale growth of the parent MCS from central Indiana through southeastern Ohio (Figs. 8a–c and 9a–c). The simulated surface cold-pool intensity (Figs. 9a–c) and, hence, surface wind speeds (not shown) are, however, still weaker than LIGHT (Figs. 6d–f). When data from the KILX radar are added (i.e., 4RAD+ILX), the forecast resembles that of ALL with a spurious storm cluster of similar intensity developing in southeastern Indiana (as defined by θ'; Figs. 8d–f and 9d–f), leading to a southeastward displacement of the simulated MCS at 6-h forecast (cf. Figs. 9f and 9c). Based on these two sensitivity tests, it is likely that the KILX radar led to the inaccurate forecast in ALL. Confirming this, when KLOT is added instead (i.e., 4RAD+LOT), the spurious storm cluster is eliminated, leading to an improved forecast similar to 4RAD (Figs. 8g–i and 9g–i). In 4RAD+LOT, however, Fig. 9h reveals a slight southward extension of the +7.5- to +10-K θ' contours in central Indiana surrounding a faint hint of an arc of lower θ' (~+1 K). This suggests that the local environment ahead of the parent MCS in central Indiana is changed in a similar fashion to 4RAD and 4RAD+ILX, but that it does not quite lead to CI and upscale growth. This result supports that while the predictability of the derecho as a whole is large throughout the suite of simulations conducted, one specific aspect of its evolution appears to be tied to smaller-scale details that are more difficult to measure (and thus inherently decreasing predictability). Albeit weaker than LIGHT, 4RAD also shows evidence of a warm tongue of surface θ' values exceeding +5 K behind the MCS's leading edge at 500 m MSL (not shown) arising from adiabatic warming within a descending RIJ.

c. *Test with assimilation of selected KILX observations*

This second group of three 3DVAR initialization sensitivity tests aims at determining whether the spurious CI may be traced back to assimilated radial velocity, radar reflectivity, or both. In these experiments, 3DVAR is used with only one radar at a time when the data assimilation is suspected of introducing spurious CI (either KILX or KLOT) to further isolate the source of forecast error. Note that prior to conducting those tests, the quality-controlled data from the latter two radars were perused at all levels and revealed no obvious nonphysical signals (e.g., hypothetically erroneous dealiasing; not shown).

Informed by the previous set of experiments (e.g., Figs. 8 and 9) and performing a 3DVAR test in which both wind and reflectivity data are assimilated from KILX only (run ILX), the spurious convection in southeastern Indiana is expected to be forecasted by ILX as

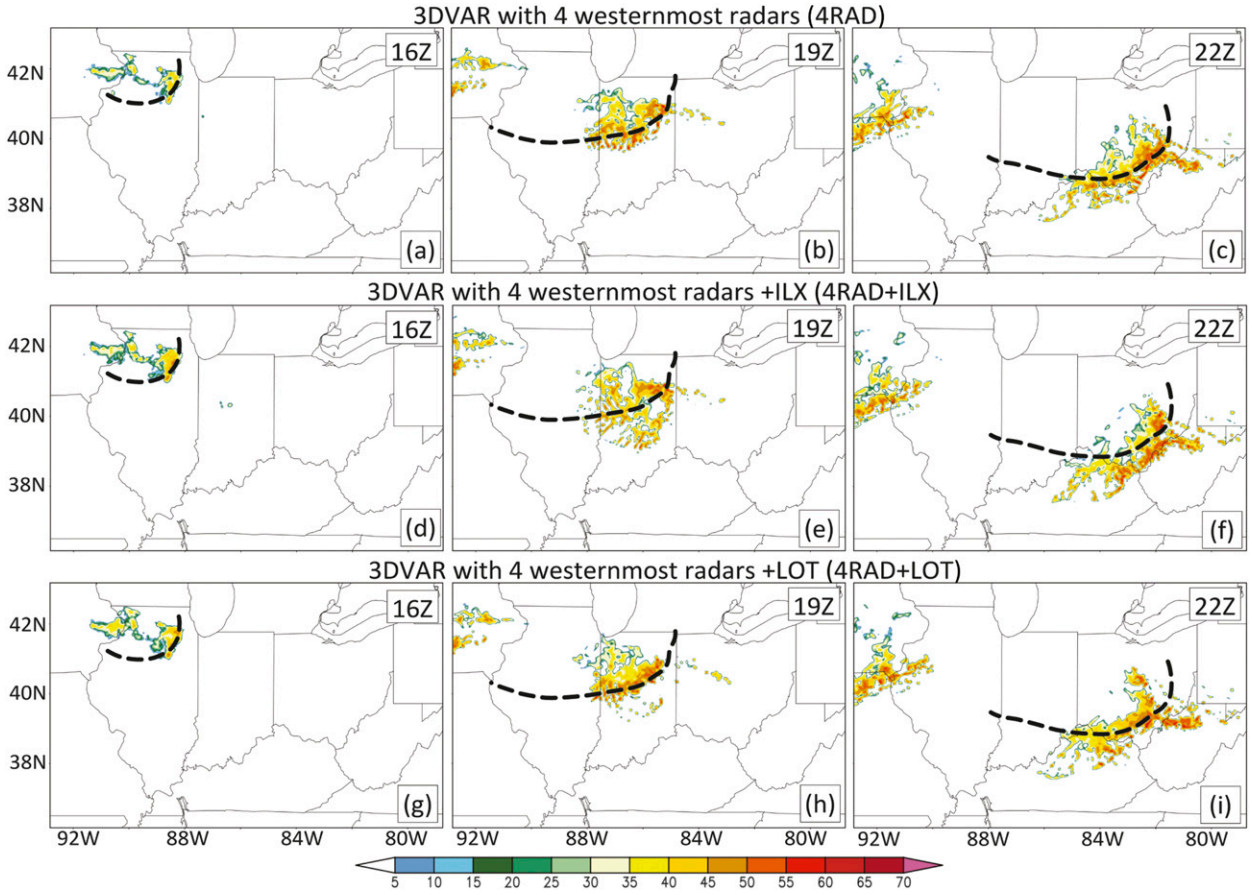

FIG. 8. As in Fig. 5, but for (a)–(c) 4RAD. (d)–(f) As in (a)–(c), but for 4RAD+ILX. (g)–(i) As in (a)–(c), but for 4RAD+LOT.

previously for 4RAD+ILX (cf. Figs. 6g–i, 9d–f, and 10a–c). When incorporating only KILX observations and excluding radial velocity from the 3DVAR assimilation (run ILX-DBZ), the forecast is somewhat unexpectedly improved and similar to 4RAD in terms of cold-pool intensity, areal coverage and location (cf. Figs. 10d–f and 9a–c), and radar reflectivity structure (not shown). In contrast, when only KILX radial velocity is assimilated (run ILX-VR), the 3-h forecast only shows spurious storms developing in southeastern Indiana (Fig. 10h) with no convection seen within the forecast domain at the analysis time (Fig. 10g). These tests that vary the KILX-only data assimilation collectively demonstrate that the inaccurate forecast in ALL (and, hence, 4RAD+ILX) arises primarily from assimilating level II radial winds from the KILX radar. Note that level I data were not tested because they were deemed too coarse to adequately resolve the cloud-scale wind field.

To help determine what potential factors in the model environment may have contributed to the simulation in developing spurious convection ahead of the MCS path near 1600 UTC, forecast model soundings from the WRF run ILX (referred to as the ILX-based or model sounding) at the nearest grid point from the Wilmington NWS sounding site (ILN; Figs. 11a–c) are compared side by side with the 1800 UTC special ILN sounding (Fig. 11d). Before pursuing this comparison, it is relevant to mention that additional 1600–1800 UTC model soundings (not shown) for CTRL, ILX-VR, and ILX-DBZ at ILN and in central Indiana away from potential spurious CI exhibit very similar thermodynamic profiles to the ILX soundings in Figs. 11a–c (MLCIN near 15 J kg^{-1} and MLCAPE around 4000 J kg^{-1}). This similarity indicates that the pre-MCS mesoscale environment in WRF is fairly homogeneous around ILN and that the collective ILX soundings at ILN in Fig. 11 are representative of the prederecho environment in the simulations herein.

The ILX-based sounding has comparably smaller MLCIN and higher MLCAPE values than the RAP analysis. In particular, the 1800 UTC ILX-based sounding MLCIN and MLCAPE values (8 and 4344 J kg^{-1}, respectively) are quite different from the observed MLCIN and MLCAPE results (90 and 3408 J kg^{-1}, respectively; cf. Fig. 11c and 11d). A +0.8-K warm bias of potential

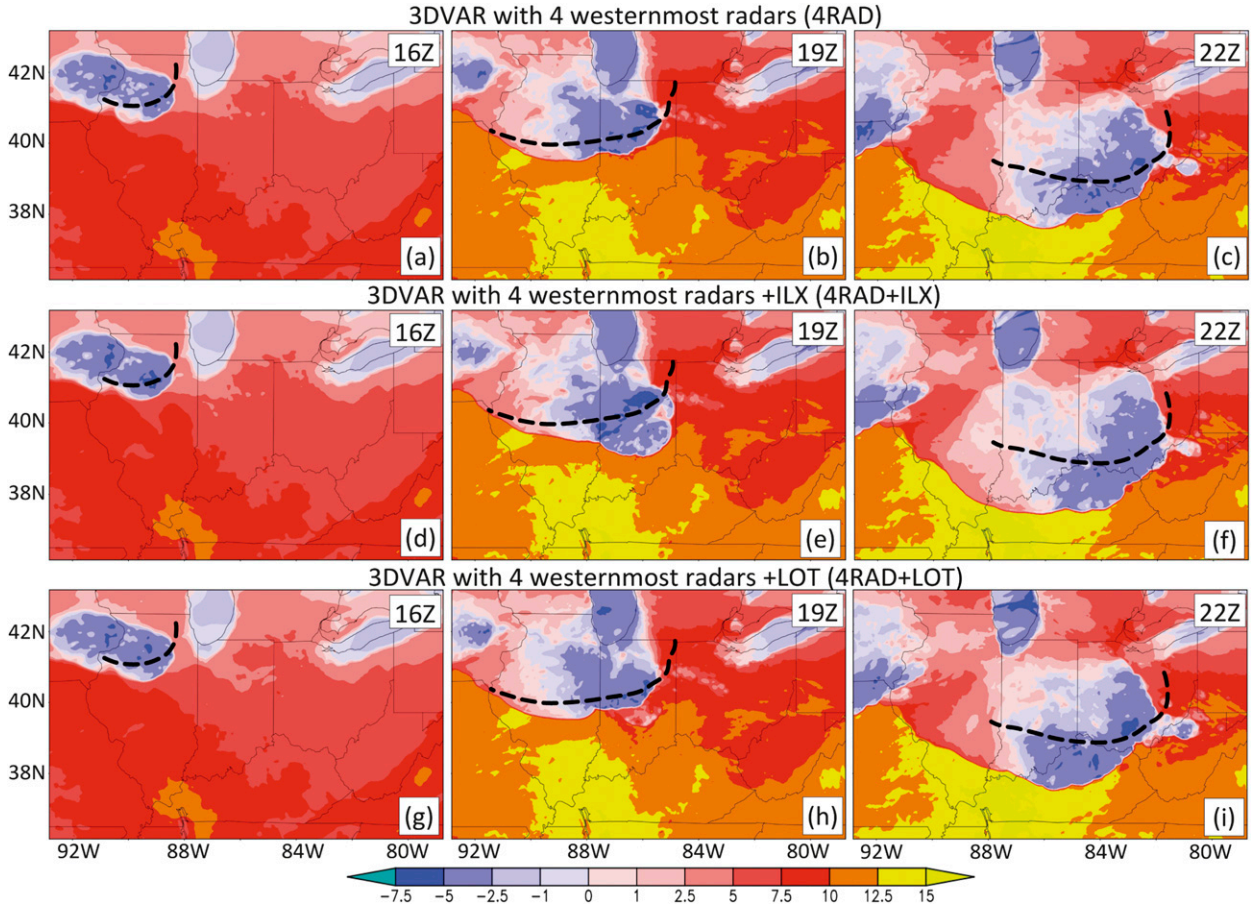

FIG. 9. As in Fig. 6, but for the 3DVAR runs of Fig. 8.

temperature and a $+2.6\,g\,kg^{-1}$ moist bias of water vapor mixing ratio in the boundary layer and a significantly weaker modeled capping inversion all contribute to the local model sounding parameter errors (e.g., Crook 1996). These model temperature and humidity errors are broadly comparable to error levels in RAP (formerly the Rapid Update Cycle or RUC) analyses reported by Coniglio (2012). The relatively small MLCIN and large MLCAPE values in the 1800 UTC model sounding suggest that some combination of errors from the initializing National Centers for Environmental Prediction (NCEP) NAM analysis (also noted in the RAP analysis) and the subsequent model forecast locally may have overdone the destabilization of the boundary layer by early afternoon in the derecho MCS's path in Indiana and Ohio regardless of whether the small-scale triggering perturbations induced from the assimilation KILX velocity data were real or spurious.

Furthermore, the 1800 UTC model sounding at ILN contained considerably stronger upper-tropospheric wind speeds of up to $30\,m\,s^{-1}$ (cf. Figs. 11c and 11d), which in turn may conceivably also have augmented the tendency for upper-tropospheric shear-induced overturning to enhance deep lifting (e.g., Coniglio et al. 2006) at the leading edge of the simulated MCS in this case.

d. Test with one 3DVAR cycle

For real-time daily forecasts over large domains (e.g., CONUS) at similar convection-allowing scales (i.e., $\leq$4 km), the use of several 3DVAR cycles is considered impractical owing to their cumulative large computational cost. For instance, the Center of Analysis and Prediction of Storms (CAPS) in Norman, Oklahoma, routinely makes use of only one 3DVAR cycle at the analysis time prior to conducting convection-allowing forecasts over CONUS. This method is by design aimed at significantly reducing total computational costs and has been shown to be relatively efficient in improving the forecasts of high-impact weather events (e.g., Gao et al. 2013). To mimic the CAPS real-time, convection-allowing analyses and forecasts, an additional simulation was conducted in which 3DVAR was only applied for consistency at the analysis time herein (1600 UTC). The 4RAD simulation was selected for this test because

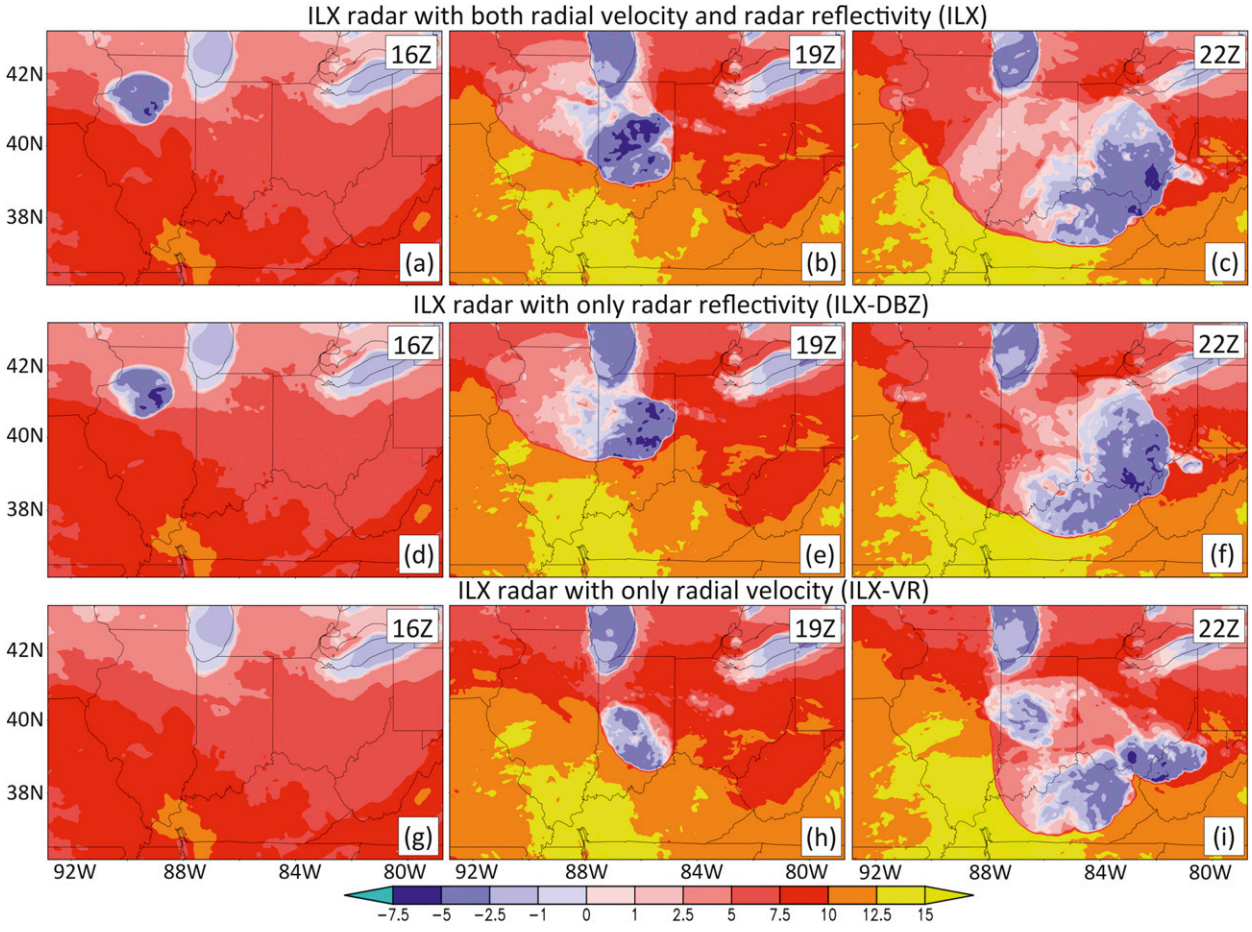

FIG. 10. As in Fig. 9, but for (a)–(c) the ILX 3DVAR run. (d)–(f) As in (a)–(c), but for ILX-dB*Z*. (g)–(i) As in (a)–(c), but for ILX-VR.

it produced the best overall forecast of the 3DVAR experiments (Figs. 6g–i and 9) and was found to be the most computationally efficient (as it uses only four radars). The forecast shows a broadly high degree of similarity to the original 3DVAR run in terms of both radar reflectivity structure (cf. Figs. 12a–c and 8a–c) and the intensity and areal coverage of the cold pool (cf. Figs. 12d–f and 9a–c) and 10-m wind speeds (Figs. 12g–i, not shown for 4RAD), further confirming the hypothesis that one 3DVAR cycle would be sufficient to initialize this particular case study forecast. A major difference seen when using only one instead of multiple 3DVAR cycles is that the cold pool at analysis time primarily contains information from the background field, which in this case is the CTRL model output at 1600 UTC (cf. Figs. 12d and 6a). The forced storms nevertheless quickly generate their own cold pools and subsequently evolve into a mature derecho MCS, as in 4RAD. Owing to the resulting delay in forming a mature cold pool when using only one 3DVAR cycle, the simulated MCS at 1900 and 2200 UTC is located farther west than 4RAD by about 100 km and has a better north–south location in northern Kentucky (cf. Figs. 9b,c and 12e,f).

5. Summary

Using WRF-ARW, a computationally inexpensive lightning nudging scheme and a three-dimensional variational technique (or 3DVAR) that assimilated conventional WSR-88D data were evaluated for the forecast of the 29–30 June 2012 derecho case. As expected, the overall radar reflectivity structure of the embryonic MCS at analysis time was in better agreement with the observations when 3DVAR was utilized (e.g., Gao et al. 2013). The subsequent 3- and 6-h forecasts, however, showed better agreement with the radar reflectivity observations when total lightning data was assimilated. These results are in line with previous studies that have demonstrated noticeable improvements in mesoscale forecast skill within the 0–6-h period using 3DVAR radar-based data assimilation techniques (e.g.,

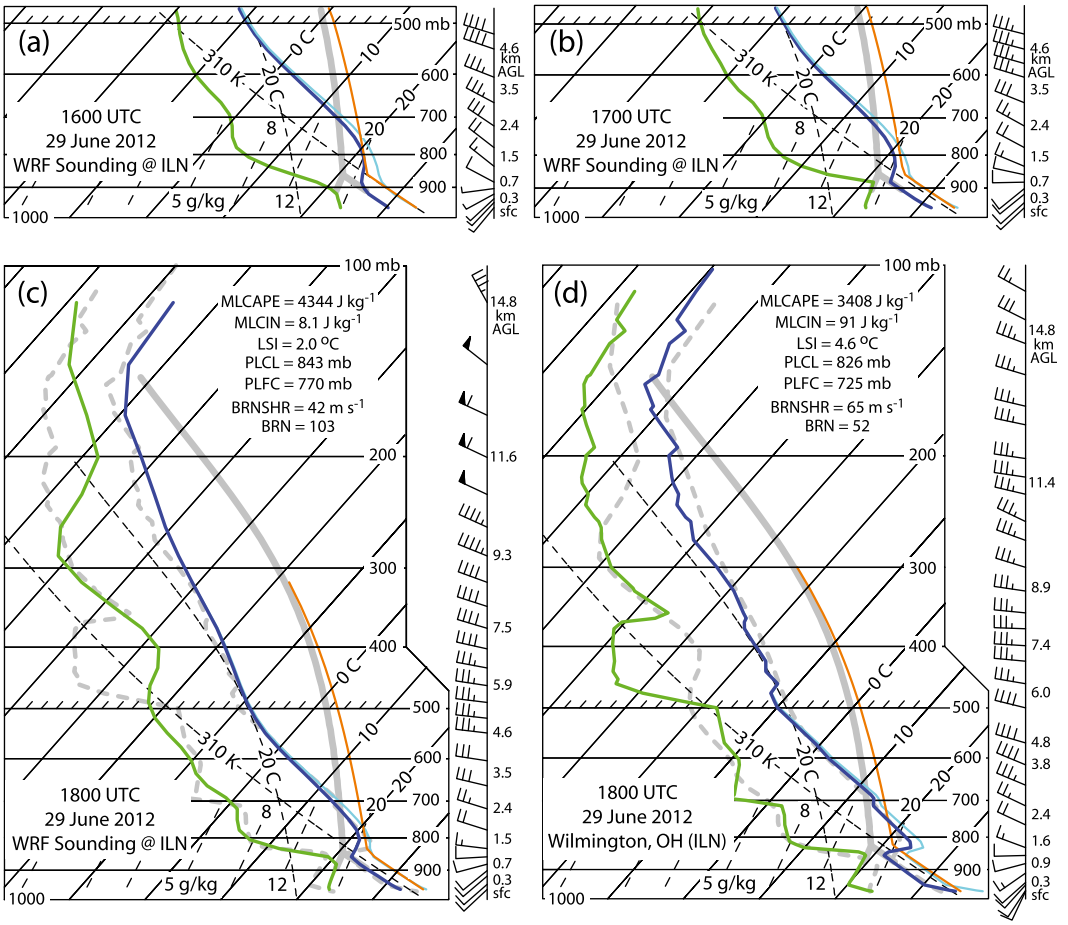

FIG. 11. Skew T–log$p$ plots depicting hourly evolution of WRF-forecast soundings on 29 Jun 2012 in the closest grid column to the ILN NWS radiosonde site at (a) 1600, (b) 1700, and (c) 1800 UTC in comparison with (d) the ILN special sounding at 1800 UTC. The mixed-layer sounding parameters (MLCAPE, MLCIN) in (c) and (d) are computed through the lowest 90 mb, which characterizes the deepening convective boundary layer. The cyan and orange curves are the virtual temperature profiles of the environment and the lifted parcel, respectively (i.e., from which the integrated virtual buoyancy is derived to compute MLCAPE and MLCIN). Wind vectors are plotted with full barb = 5 m s^{-1}, half barb = 2.5 m s^{-1}, and filled triangle = 25 m s^{-1}. The gray dashed curves in (c) correspond to the observed sounding in (d), while the gray dashed curves in (d) correspond to the model sounding in (c). The NWS operational sounding site at ILN is shown by a white-filled black circle in Figs. 1 and 2.

Hu et al. 2006a,b; Gao and Stensrud 2012; Ge et al. 2012; Gao et al. 2013) or lightning data (e.g., Alexander et al. 1999; Mansell et al. 2007; Pessi and Businger 2009). This improvement may be attributed to a better representation of the mesoscale and convective-scale cold pools (e.g., Mansell et al. 2007) or the midtropospheric heating profiles and associated cell-scale circulations from the assimilation-induced convection (Fierro et al. 2012; Gao et al. 2013) at the analysis time.

A suite of sensitivity tests was conducted to identify the primary factor(s) responsible for the formation of a spurious cluster of storms ahead of the parent MCS that led to the degradation of the forecast in the original 3DVAR simulation. These tests revealed that the assimilation of the radial velocity of the KILX radar was the chief cause, despite the actual data not exhibiting obvious nonphysical signals. Although being a single case study, this work highlights the possible encouraging role of assimilating total lightning data toward improving short-term forecasts of mesoscale convective systems, particularly given its relatively lower computational cost. The lightning assimilation is conducted at runtime, which also alleviates the need for conducting cycle forecast run(s) prior to and at the analysis time.

Additional work is planned to focus on establishing meaningful statistics of the performance of the lightning assimilation scheme at the cloud scale (4 km) over CONUS (Kain et al. 2010; Clark et al. 2012) during the

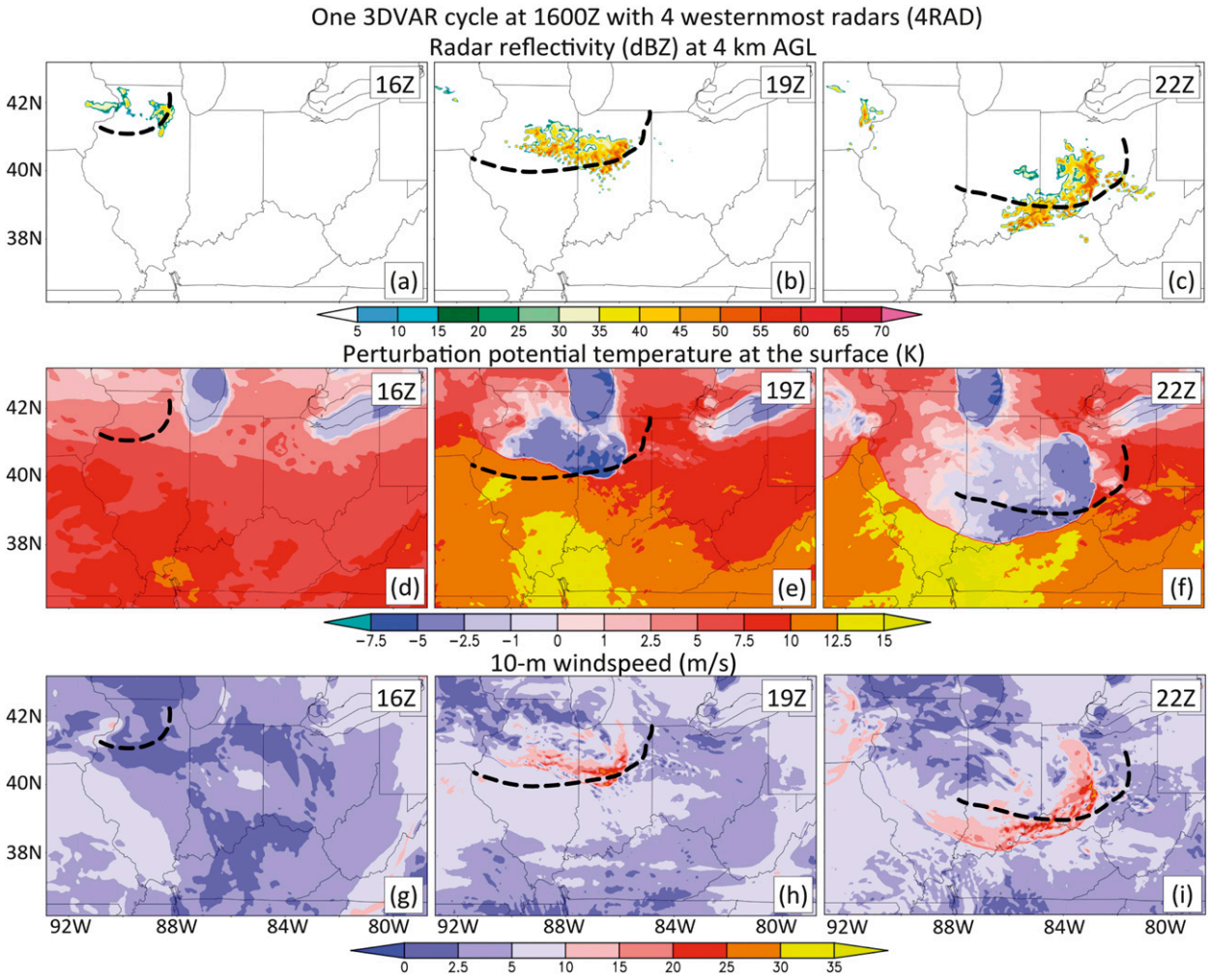

FIG. 12. Results for one assimilation cycle at 1600 UTC employing only the four westernmost radars (4RAD): (a)–(c) as in Figs. 8, (d)–(f) as in Fig. 9, and (g)–(i) as in Fig. 7. Legends for colors and shadings are shown at the bottom of each row.

course of the 2013 spring and early summer seasons. The distribution of convection during the warm season may be expected to include many thunderstorm days and span various convective regimes including isolated storms, MCSs, and landfalling mesoscale tropical convective systems. Some recent preliminary results of convection-allowing model forecasts initialized at 0000 UTC during the 2013 warm season suggest that the lightning assimilation technique seems to perform best on days favorable for the development of nocturnal MCSs. The reasons for this behavior are threefold: (i) climatologically, nocturnal MCSs often initiate/form within the 0000–0200 UTC period when lightning data were assimilated; (ii) the large-scale environment is usually depicted well by the reanalysis (including the nocturnal low-level jet); and (iii) the upscale evolution and placement of MCSs are strongly dictated by the initial placement and intensity of convectively induced cold pools. These findings collectively hold the promise of helping to provide improved operational CONUS-scale human and numerical weather forecasts, since as noted in the introduction MCSs often produce damaging winds, copious cloud-to-ground lightning, and heavy rainfall over significant areas.

Acknowledgments. The authors gratefully acknowledge the efforts of three anonymous formal reviewers, whose comments and suggestions helped to improve the revised manuscript. The authors also thank Ami Arthur for providing the NSSL three-dimensional NMQ radar mosaic data, and are also grateful to Kevin Manross, Travis Smith, and Christopher Riedel for providing the RAP analysis data. Thanks also go out to Bill Callahan, Benny Chukrun, Stan Heckman, and Jim Anderson from Earth Networks for providing the total lightning

data. Funding was provided by NOAA/Office of Oceanic and Atmospheric Research under NOAA–University of Oklahoma Cooperative Agreement NA11OAR4320072, U.S. Department of Commerce. This work was further supported by the NESDIS program, which operates under the auspices of the National Oceanic and Atmospheric Administration of the U.S. Department of Commerce under the Grant NOAA-NESDIS-OAR-NA08OAR4320904. Computer resources were provided by the Oklahoma Supercomputing Center for Education and Research (OSCER) hosted at the University of Oklahoma.

REFERENCES

Aksoy, A., D. C. Dowell, and C. Snyder, 2009: A multicase comparative assessment of the ensemble Kalman filter for assimilation of radar observations. Part I: Storm-scale analyses. *Mon. Wea. Rev.,* **137,** 1805–1824.

Albers, S. C., J. A. McGinley, D. L. Birkenheuer, and J. R. Smart, 1996: The Local Analysis and Prediction System (LAPS): Analyses of clouds, precipitation, and temperature. *Wea. Forecasting,* **11,** 273–287.

Alexander, G. D., J. A. Weinman, V. Karyampudi, W. S. Olson, and A. C. L. Lee, 1999: The effect of assimilating rain rates derived from satellites and lightning on forecasts of the 1993 Superstorm. *Mon. Wea. Rev.,* **127,** 1433–1457.

Barker, D. M., W. Huang, Y.-R. Guo, A. J. Bourgeois, and Q. N. Xiao, 2004: A three-dimensional variational data assimilation system for MM5: Implementation and initial results. *Mon. Wea. Rev.,* **132,** 897–914.

Benjamin, S. G., and Coauthors, 2004: An hourly assimilation–forecast cycle: The RUC. *Mon. Wea. Rev.,* **132,** 495–518.

Boccippio, D. J., K. L. Cummins, H. J . Christian, and S. J. Goodman, 2001: Combined satellite- and surface-based estimation of the intracloud–cloud-to-ground lightning ratio over the continental United States. *Mon. Wea. Rev.,* **129,** 108–122.

Brewster, K., 2002: Recent advances in the diabatic initialization of a non-hydrostatic numerical model. Preprints, *19th Conf. on Weather Analysis and Forecasting/15th Conf. on Numerical Weather Prediction/21st Conf. on Severe Local Storms,* San Antonio, TX, Amer. Meteor. Soc., J6.3. [Available online at https://ams.confex.com/ams/pdfpapers/47414.pdf.]

Bryan, G. H., and H. Morrison, 2012: Sensitivity of a simulated squall line to horizontal resolution and parameterization of microphysics. *Mon. Wea. Rev.,* **140,** 202–225.

Chang, D.-E., J. A. Weinman, C. A. Morales, and W. S. Olson, 2001: The effect of spaceborne microwave and ground-based continuous lightning measurements on forecasts of the 1998 Groundhog Day storm. *Mon. Wea. Rev.,* **129,** 1809–1833.

Chen, F., and J. Dudhia, 2001: Coupling an advanced land surface–hydrology model with the Penn State–NCAR MM5 modeling system. Part I: Model implementation and sensitivity. *Mon. Wea. Rev.,* **129,** 569–585.

——, Z. Janjić, and K. Mitchell, 1997: Impact of atmospheric surface-layer parameterizations in the new land-surface scheme of the NCEP mesoscale Eta Model. *Bound.-Layer Meteor.,* **85,** 391–421.

Clark, A. J., and Coauthors, 2012: An overview of the 2010 Hazardous Weather Testbed Experimental Forecast Program Spring Experiment. *Bull. Amer. Meteor. Soc.,* **93,** 55–74.

Coniglio, M. C., 2012: Verification of RUC 0–1-h forecasts and SPC mesoscale analyses using VORTEX2 soundings. *Wea. Forecasting,* **27,** 667–683.

——, D. J. Stensrud, and M. B. Richman, 2004: An observational study of derecho-producing convective systems. *Wea. Forecasting,* **19,** 320–337.

——, ——, and L. J. Wicker, 2006: Effects of upper-level shear on the structure and maintenance of strong quasi-linear mesoscale convective systems. *J. Atmos. Sci.,* **63,** 1231–1252.

Cotton, W. R., 1999: An overview of mesoscale convective systems. *Storms,* R. Pielke Jr. and R. Pielke Sr., Eds., Vol. 2, Routledge Press, 3–25.

Crook, N. A., 1996: Sensitivity of moist convection forced by boundary-layer processes to low-level thermodynamic fields. *Mon. Wea. Rev.,* **124,** 1767–1785.

Deierling, W., and W. A. Petersen, 2008: Total lightning activity as an indicator of updraft characteristics. *J. Geophys. Res.,* **113,** D16210, doi:10.1029/2007JD009598.

Ek, M. B., K. E. Mitchell, Y. Lin, E. Rogers, P. Grunmann, V. Koren, G. Gayno, and J. D. Tarpley, 2003: Implementation of Noah land surface model advances in the National Centers for Environmental Prediction operational mesoscale Eta Model. *J. Geophys. Res.,* **108,** 8851, doi:10.1029/2002JD003296.

Etherton, B. J., and C. H. Bishop, 2004: Resilience of hybrid ensemble/3DVAR analysis schemes to model error and ensemble covariance error. *Mon. Wea. Rev.,* **132,** 1065–1080.

Evensen, G., 1994: Sequential data assimilation with a nonlinear quasi-geostrophic model using Monte Carlo methods to forecast error statistics. *J. Geophys. Res.,* **99,** 10 143–10 162.

——, 2003: The ensemble Kalman filter: Theoretical formulation and practical implementation. *Ocean Dyn.,* **53,** 343–367.

Fierro, A. O., and J. M. Reisner, 2011: High-resolution simulation of the electrification and lightning of Hurricane Rita during the period of rapid intensification. *J. Atmos. Sci.,* **68,** 477–494.

——, M. S. Gilmore, E. R. Mansell, L. J. Wicker, and J. M. Straka, 2006: Electrification and lightning in an idealized boundary-crossing supercell simulation of 2 June 1995. *Mon. Wea. Rev.,* **134,** 3149–3172.

——, E. Mansell, C. Ziegler, and D. MacGorman, 2012: Application of a lightning data assimilation technique in the WRF-ARW model at cloud-resolving scales for the tornado outbreak of 24 May 2011. *Mon. Wea. Rev.,* **140,** 2609–2627.

Fritsch, J. M., R. J. Kain, and C. R. Chelius, 1986: The contribution of mesoscale convective weather systems to the warm-season precipitation in the United States. *J. Climate Appl. Meteor.,* **25,** 1333–1345.

Gao, J., and D. J. Stensrud, 2012: Assimilation of reflectivity data in a convective-scale, cycled 3DVAR framework with hydrometeor classification. *J. Atmos. Sci.,* **69,** 1054–1065.

——, M. Xue, A. Shapiro, and K. K. Droegemeier, 1999: A variational method for the retrieval of three-dimensional wind fields from dual-Doppler radars. *Mon. Wea. Rev.,* **127,** 2128–2142.

——, ——, K. Brewster, and K. K. Droegemeier, 2004: A three-dimensional variational data assimilation method with recursive filter for single-Doppler radar. *J. Atmos. Oceanic Technol.,* **21,** 457–469.

——, and Coauthors, 2013: A real-time weather-adaptive 3DVAR analysis system for severe weather detections and warnings. *Wea. Forecasting,* **28,** 727–745.

Gauthier, P., M. Tanguay, S. Laroche, S. Pellerin, and J. Morneau, 2007: Extension of 3DVAR to 4DVAR: Implementation of 4DVAR at the Meteorological Service of Canada. *Mon. Wea. Rev.,* **135,** 2339–2354.

Ge, G., J. Gao, K. A. Brewster, and M. Xue, 2010: Effects of beam broadening and earth curvature in radar data assimilation. *J. Atmos. Oceanic Technol.,* **27,** 617–636.

——, ——, and M. Xue, 2012: Diagnostic pressure equation as a weak constraint in a storm-scale three dimensional variational radar data assimilation system. *J. Atmos. Oceanic Technol.,* **29,** 1075–1092.

Godinez, H. C., J. M. Reisner, A. O. Fierro, S. R. Guimond, and J. Kao, 2012: Determining key model parameters of rapidly intensifying Hurricane Guillermo (1997) using the ensemble Kalman filter. *J. Atmos. Sci.,* **69,** 3147–3171.

Goodman, S. J., and D. R. MacGorman, 1986: Cloud-to-ground lightning activity in mesoscale convective complexes. *Mon. Wea. Rev.,* **114,** 2320–2328.

——, and Coauthors, 2013: The GOES-R Geostationary Lightning Mapper (GLM). *Atmos. Res.,* **125–126,** 34–49.

Gurka, J. J., T. A. Schmit, T. M. Renkevens, M. M. Gunshor, and J. Li, 2006: 2006 update on baseline instruments for GOES-R series. *Atmospheric and Environmental Remote Sensing Data Processing and Utilization II: Perspective on Calibration/ Validation Initiatives and Strategies,* A. H. L. Huang and H. J. Bloom, Eds., International Society for Optical Engineering (SPIE Proceedings, Vol. 6301), 63010H, doi:10.1117/12.683701.

Hong, S.-Y., and J.-O. J. Lim, 2006: The WRF single-moment microphysics scheme (WSM6). *J. Korean Meteor. Soc.,* **42,** 129–151.

Houtekamer, P. L., and H. Mitchell, 1998: Data assimilation using an ensemble Kalman filter technique. *Mon. Wea. Rev.,* **126,** 796–811.

Houze, R. A., Jr., 1993: *Cloud Dynamics.* Academic Press, 573 pp.

——, B. F. Smull, and P. Dodge, 1990: Mesoscale organization of springtime rainstorms in Oklahoma. *Mon. Wea. Rev.,* **118,** 613–654.

Hsiao, L.-F., D.-S. Chen, Y.-H. Kuo, Y.-R. Guo, T.-C. Yeh, J.-S. Hong, C.-T. Fong, and C.-S. Lee, 2012: Application of WRF 3DVAR to operational typhoon prediction in Taiwan: Impact of outer loop and partial cycling approaches. *Wea. Forecasting,* **27,** 1249–1263.

Hu, M., M. Xue, and K. Brewster, 2006a: 3DVAR and cloud analysis with WSR-88D level-II data for the prediction of the Fort Worth, Texas, tornadic thunderstorms. Part I: Cloud analysis and its impact. *Mon. Wea. Rev.,* **134,** 675–698.

——, ——, J. Gao, and K. Brewster, 2006b: 3DVAR and cloud analysis with WSR-88D level-II data for the prediction of the Fort Worth, Texas, tornadic thunderstorms. Part II: Impact of radial velocity analysis via 3DVAR. *Mon. Wea. Rev.,* **134,** 699–721.

Janjić, Z. I., 1994: The step-mountain eta coordinate model: Further developments of the convection, viscous sublayer, and turbulence closure schemes. *Mon. Wea. Rev.,* **122,** 927–945.

Johns, R. H., and W. D. Hirt, 1987: Derechos: Widespread convectively induced windstorms. *Wea. Forecasting,* **2,** 32–49.

——, and C. A. Doswell III, 1992: Severe local storms forecasting. *Wea. Forecasting,* **7,** 588–612.

Jones, C. D., and B. Macpherson, 1997a: A latent heat nudging scheme for the assimilation of precipitation data into an operational mesoscale model. *Meteor. Appl.,* **4,** 269–277.

——, and ——, 1997b: Sensitivity of the limited area model to the assimilation of precipitation estimates derived from lightning data. UKMO Forecasting Research Tech. Rep. 212, 11 pp.

Kain, J. S., and J. M. Fritsch, 1993: Convective parameterization for mesoscale models: The Kain–Fritsch scheme. *The Representation of Cumulus Convection in Numerical Models, Meteor. Monogr.,* No. 46, Amer. Meteor. Soc., 165–170.

——, S. R. Dembeck, S. J. Weiss, J. L. Case, J. J. Levit, and R. A. Sobash, 2010: Extracting unique information from high- resolution forecast models: Monitoring selected fields and phenomena every time step. *Wea. Forecasting,* **25,** 1536–1542.

Li, Y., X. Wang, and M. Xue, 2012: Assimilation of radar radial velocity data with the WRF hybrid ensemble–3DVAR system for the prediction of Hurricane Ike (2008). *Mon. Wea. Rev.,* **140,** 3507–3524.

MacGorman, D. R., D. W. Burgess, V. Mazur, W. D. Rust, W. L. Taylor, and B. C. Johnson, 1989: Lightning rates relative to tornadic storm evolution on 22 May 1981. *J. Atmos. Sci.,* **46,** 221–251.

Maddox, R. A., 1983: Large-scale meteorological conditions associated with midlatitude, mesoscale convective complexes. *Mon. Wea. Rev.,* **111,** 1475–1493.

Mansell, E. R., C. L. Ziegler, and D. R. MacGorman, 2007: A lightning data assimilation technique for mesoscale forecast models. *Mon. Wea. Rev.,* **135,** 1732–1748.

Mellor, G. L., and T. Yamada, 1982: Development of turbulence closure model for geophysical fluid problems. *Rev. Geophys. Space Phys.,* **20,** 851–875.

Meng, Z., and F. Zhang, 2008a: Tests of an ensemble Kalman filter for mesoscale and regional-scale data assimilation. Part III: Comparison with 3DVAR in a real-data case study. *Mon. Wea. Rev.,* **136,** 522–540.

——, and ——, 2008b: Tests of an ensemble Kalman filter for mesoscale and regional-scale data assimilation. Part IV: Comparison with 3DVAR in a month-long experiment. *Mon. Wea. Rev.,* **136,** 3671–3682.

Mlawer, E., S. Taubman, P. Brown, M. Iacono, and S. Clough, 1997: Radiative transfer for inhomogeneous atmospheres: RRTM, a validated correlated-*k* model for the longwave. *J. Geophys. Res.,* **102** (D14), 16 663–16 682.

Papadopoulos, A., T. G. Chronis, and E. N. Anagnostou, 2005: Improving convective precipitation forecasting through assimilation of regional lightning measurements in a mesoscale model. *Mon. Wea. Rev.,* **133,** 1961–1977.

Passarelli, R. E., Jr., 1978: An approximate analytical model of the vapor deposition and aggregation growth of snowflakes. *J. Atmos. Sci.,* **35,** 118–124.

Pessi, A. T., and S. Businger, 2009: The impact of lightning data assimilation on a winter storm simulation over the North Pacific Ocean. *Mon. Wea. Rev.,* **137,** 3177–3195.

Potvin, C. K., D. Betten, L. J. Wicker, K. L. Elmore, and M. I. Biggerstaff, 2012: 3DVAR versus traditional dual-Doppler wind retrievals of a simulated supercell thunderstorm. *Mon. Wea. Rev.,* **140,** 3487–3494.

Purser, R. J., W.-S. Wu, D. F. Parrish, and N. M. Roberts, 2003a: Numerical aspects of the application of recursive filters to variational statistical analysis. Part I: Spatially homogeneous and isotropic Gaussian covariances. *Mon. Wea. Rev.,* **131,** 1524–1535.

——, ——, ——, and ——, 2003b: Numerical aspects of the application of recursive filters to variational statistical analysis. Part I: Spatially homogeneous and isotropic Gaussian covariances. *Mon. Wea. Rev.,* **131,** 1536–1548.

Rogers, R. R., and M. K. Yau, 1989: *A Short Course in Cloud Physics.* Pergamon Press, 290 pp.

Schenkman, A. D., M. Xue, A. Shapiro, K. Brewster, and J. Gao, 2011: The analysis and prediction of the 8–9 May 2007 Oklahoma tornadic mesoscale convective system by assimilating WSR-88D and CASA radar data using 3DVAR. *Mon. Wea. Rev.,* **139,** 224–246.

Skamarock, W. C., and J. B. Klemp, 2007: A time-split nonhydrostatic atmospheric model for research and NWP applications. *J. Comput. Phys.,* **227,** 3465–3485.

Stensrud, D. J., and J.-W. Bao, 1992: Behaviors of variational and nudging assimilation techniques with a chaotic low-order model. *Mon. Wea. Rev.,* **120,** 3016–3028.

——, and J. Gao, 2010: Importance of horizontally inhomogeneous environmental initial conditions to ensemble storm-scale radar data assimilation and very short-range forecasts. *Mon. Wea. Rev.,* **138,** 1250–1272.

——, and Coauthors, 2009: Convective-scale warn-on-forecast system: A vision for 2020. *Bull. Amer. Meteor. Soc.,* **90,** 1487–1499.

Van Weverberg, K., and Coauthors, 2013: The role of cloud microphysics parameterization in the simulation of mesoscale convective system clouds and precipitation in the tropical western Pacific. *J. Atmos. Sci.,* **70,** 1104–1128.

Vescio, M., and Coauthors, 2013: The historic derecho of June 29, 2012. NWS Service Assessment, National Weather Service, Silver Spring, MD, 61 pp.

Wakimoto, R. M., H. V. Murphey, A. Nester, D. P. Jorgensen, and N. T. Atkins, 2006: High winds generated by bow echoes. Part I: Overview of the Omaha bow echo 5 July 2003 storm during BAMEX. *Mon. Wea. Rev.,* **134,** 2793–2812.

Wang, X., 2011: Application of the WRF hybrid ETKF–3DVAR data assimilation system for hurricane track forecasts. *Wea. Forecasting,* **26,** 868–884.

——, C. Snyder, and T. M. Hamill, 2007: On the theoretical equivalence of differently proposed ensemble–3DVAR hybrid analysis schemes. *Mon. Wea. Rev.,* **135,** 222–227.

——, D. M. Barker, C. Snyder, and T. M. Hamill, 2008: A hybrid ETKF–3DVAR data assimilation scheme for the WRF model. Part II: Real observation experiments. *Mon. Wea. Rev.,* **136,** 5132–5147.

Wiens, K. C., S. A. Rutledge, and S. A. Tessendorf, 2005: The 29 June 2000 supercell observed during STEPS. Part II: Lightning and charge structure. *J. Atmos. Sci.,* **62,** 4151–4177.

Xiao, Q., Y.-H. Kuo, J. Sun, W.-C. Lee, E. Lim, Y.-R. Guo, and D. M. Barker, 2005: Assimilation of Doppler radar observations with a regional 3DVAR system: Impact of Doppler velocities on forecasts of a heavy rainfall case. *J. Appl. Meteor.,* **44,** 768–788.

Xu, Q., M. Xue, and K. K. Droegemeer, 1996: Numerical simulations of density currents in sheared environments within a vertically confined channel. *J. Atmos. Sci.,* **53,** 770–786.

Xue, M., Q. Xu, and K. K. Droegemeier, 1997: A theoretical and numerical study of density currents in nonconstant shear flows. *J. Atmos. Sci.,* **54,** 1998–2019.

——, and Coauthors, 2001: The Advanced Regional Prediction System (ARPS)—A multiscale nonhydrostatic atmospheric simulation and prediction tool. Part II: Model physics and applications. *Meteor. Atmos. Phys.,* **76,** 134–165.

——, D. Wang, J. Gao, K. Brewster, and K. K. Droegemeier, 2003: The Advanced Regional Prediction System (ARPS), storm-scale numerical weather prediction and data assimilation. *Meteor. Atmos. Phys.,* **76,** 143–165.

Zhang, F., 2005: Dynamics and structure of mesoscale error covariance of a winter cyclone estimated through short-range ensemble forecasts. *Mon. Wea. Rev.,* **133,** 2876–2893.

——, Y. Weng, J. A. Sippel, Z. Meng, and C. H. Bishop, 2009: Cloud-resolving hurricane initialization and prediction through assimilation of Doppler radar observations with an ensemble Kalman filter. *Mon. Wea. Rev.,* **137,** 2105–2125.

Zhang, J., F. Carr, and K. Brewster, 1998: ADAS cloud analysis. Preprints, *12th Conf. on Numerical Weather Prediction,* Phoenix, AZ, Amer. Meteor. Soc., 185–188.

——, and Coauthors, 2011: National Mosaic and Multi-Sensor QPE (NMQ) system: Description, results, and future plans. *Bull. Amer. Meteor. Soc.,* **92,** 1321–1338.

Zhang, S., T. Li, X. Ge, M. Peng, and N. Pan, 2012: A 3DVAR-based dynamical initialization scheme for tropical cyclone predictions. *Wea. Forecasting,* **27,** 473–483.

Ziegler, C., 1999: Issues in forecasting mesoscale convective systems: An observational and modeling perspective. *Storms,* R. Pielke Jr. and R. Pielke Sr., Eds., Vol. 2, Routledge Press, 26–42.

——, E. Mansell, J. Straka, D. MacGorman, and D. Burgess, 2010: The impact of spatial variations of low-level stability on the life cycle of a simulated supercell storm. *Mon. Wea. Rev.,* **138,** 1738–1766.